

1 **Multiple 9-1-1 complexes promote homolog synapsis, DSB repair, and ATR  
2 signaling during mammalian meiosis**

3  
4 Catalina Pereira<sup>1</sup>, Gerardo A. Arroyo-Martinez<sup>1</sup>, Matthew Z. Guo<sup>1</sup>, Michael S. Downey<sup>1</sup>,  
5 Emma R. Kelly<sup>2</sup>, Kathryn J. Grive<sup>3</sup>, Shantha K. Mahadevaiah<sup>4</sup>, Jennie Sims<sup>5</sup>, Vitor Marcel  
6 Faça<sup>6</sup>, Charlton Tsai<sup>1</sup>, Carl J. Schiltz<sup>1</sup>, Niek Wit<sup>7</sup>, Heinz Jacobs<sup>7</sup>, Nathan L. Clark<sup>8</sup>,  
7 Raimundo Freire<sup>9, 10, 11</sup>, James M. A. Turner<sup>4</sup>, Amy M. Lyndaker<sup>2</sup>, Miguel A. Brieño-  
8 Enríquez<sup>12</sup>, Paula E. Cohen<sup>1</sup>, Marcus B. Smolka<sup>5</sup>, and Robert S. Weiss<sup>1,\*</sup>

9  
10 <sup>1</sup>Department of Biomedical Sciences, Cornell University, Ithaca, NY, USA

11 <sup>2</sup>Division of Mathematics and Natural Sciences, Elmira College, Elmira, NY, USA

12 <sup>3</sup>Department of Obstetrics and Gynecology, Brown University, Providence, RI, USA

13 <sup>4</sup>Sex Chromosome Biology Laboratory, The Francis Crick Institute, London, UK

14 <sup>5</sup>Department of Molecular Biology and Genetics, Weill Institute for Cell and Molecular  
15 Biology, Cornell University, Ithaca, NY, USA

16 <sup>6</sup>Department of Biochemistry and Immunology, FMRP, University of São Paulo, Ribeirão  
17 Preto, SP, Brazil

18 <sup>7</sup>Division of Immunology, The Netherlands Cancer Institute, Amsterdam, The Netherlands

19 <sup>8</sup>Department of Human Genetics, University of Utah, Salt Lake City, UT, USA

20 <sup>9</sup>Unidad de Investigación, Hospital Universitario de Canarias, 38320 Tenerife, Spain

21 <sup>10</sup>Instituto de Tecnologías Biomédicas, Universidad de La Laguna, 38200, La Laguna,  
22 Tenerife, Spain

23 <sup>11</sup>Universidad Fernando Pessoa Canarias, 35450 Las Palmas de Gran Canaria, Spain

24 <sup>12</sup>Magee-Womens Research Institute, Department of Obstetrics, Gynecology and  
25 Reproductive Sciences, University of Pittsburgh, Pittsburgh, PA, USA

26 \* Corresponding author: Email: [rsw26@cornell.edu](mailto:rsw26@cornell.edu); Phone: 607-253-4443

27

28 Running title: Multiple 9-1-1 complexes function in mammalian meiosis

29

30 **ABSTRACT**

31 DNA damage response mechanisms have meiotic roles that ensure successful gamete  
32 formation. While completion of meiotic double-strand break (DSB) repair requires the  
33 canonical RAD9A-RAD1-HUS1 (9A-1-1) complex, mammalian meiocytes also express  
34 RAD9A and HUS1 paralogs, RAD9B and HUS1B, predicted to form alternative 9-1-1  
35 complexes. The RAD1 subunit is shared by all predicted 9-1-1 complexes and localizes  
36 to meiotic chromosomes even in the absence of HUS1 and RAD9A. Here we report that  
37 testis-specific RAD1 disruption resulted in impaired DSB repair, germ cell depletion and  
38 infertility. Unlike *Hus1* or *Rad9a* disruption, *Rad1* loss also caused defects in homolog  
39 synapsis, ATR signaling and meiotic sex chromosome inactivation. Comprehensive testis  
40 phosphoproteomics revealed that RAD1 and ATR coordinately regulate numerous  
41 proteins involved in DSB repair, meiotic silencing, synaptonemal complex formation, and  
42 cohesion. Together, these results establish critical roles for both canonical and alternative  
43 9-1-1 complexes in meiotic ATR activation and successful prophase I completion.

## 44 INTRODUCTION

45 DNA damage response (DDR) mechanisms protect genomic integrity by sensing  
46 and repairing DNA lesions or initiating apoptosis when lesions are unrepairable (Blackford  
47 and Jackson, 2017). DDR proteins are also essential for proper haploid gamete formation.  
48 Although double-strand DNA breaks (DSBs) are considered to be the most toxic form of  
49 DNA damage, meiotic recombination relies on SPO11-induced DSBs for homologous  
50 chromosomes to synapse, exchange genetic material, and properly segregate at the first  
51 meiotic division (Bolcun-Filas et al., 2014; Gray and Cohen, 2016). Of particular  
52 importance are the meiotic events that occur during the five sub-stages of prophase I, a  
53 major feature of which involves the transient formation of the proteinaceous structure  
54 called the synaptonemal complex (SC) (Cahoon and Hawley, 2016; Gray and Cohen,  
55 2016). During the first stage, leptotene, axial elements containing SC protein 3 (SYCP3)  
56 form along condensed chromosomes (Page and Hawley, 2004). Additionally, the DNA  
57 damage marker,  $\gamma$ H2AX, accumulates during leptotene as chromosomes experience  
58 SPO11-induced DSBs. Progression into zygotene is characterized by the pairing and  
59 synapsis of chromosomes, marked by the presence of the central element protein SC  
60 protein 1 (SYCP1). By pachynema DSB repair is completed and  $\gamma$ H2AX is no longer  
61 present on the fully synapsed autosomes. However, in male meiocytes, abundant  $\gamma$ H2AX  
62 is apparent at the sex body containing the X and Y chromosomes, which synapse only in  
63 a small domain called the pseudoautosomal region but otherwise remain unsynapsed.  
64 Meiotic cells subsequently enter diplotene, featuring dissolution of the central element  
65 while homologous chromosomes remain tethered by crossovers. Breakdown of the SC  
66 marks the final stage in prophase I, diakinesis.

67 Ataxia-telangiectasia and Rad3-related (ATR) kinase is a key regulator of  
68 recombinational DSB repair and synapsis throughout meiotic prophase I (Pereira et al.,  
69 2020). ATR activation in somatic cells has been well characterized; however, the  
70 mechanisms of meiotic ATR activation have not been fully elucidated. ATR activation in  
71 response to replication stress and other signals in mitotic cells is known to involve  
72 interaction between the RAD9A-RAD1-HUS1 (9A-1-1) complex and Topoisomerase 2-  
73 Binding Protein I (TOPBP1) (Blackford and Jackson, 2017). The toroidal, PCNA-like 9A-  
74 1-1 complex is loaded at recessed DNA ends by the RAD17- Replication Factor C (RFC)  
75 clamp loader (Eichinger and Jentsch, 2011). ATR in association with ATR Interacting  
76 Protein (ATRIP) independently localizes to Replication Protein A (RPA)-coated single  
77 stranded DNA (Zou, 2003)The 9A-1-1 complex then interacts with the RAD9A-RAD1-  
78 HUS1 Interacting Nuclear Orphan (RHINO) and TOPBP1, which allows TOPBP1 to  
79 activate ATR via its ATR-activating domain (Cotta-Ramusino et al., 2011; Delacroix et al.,  
80 2007; Lindsey-Boltz et al., 2015) ATR activation initiates several downstream processes  
81 such as cell cycle arrest, DNA repair, fork stabilization, and inhibition of new origin firing,  
82 or triggers apoptosis (Saldivar et al., 2017). Independent of 9A-1-1/TOPBP1, ATR also  
83 can be directly activated during a normal mitotic cell cycle by Ewing's Tumor Associated-  
84 antigen 1 (ETAA1), in part to promote metaphase chromosome alignment and spindle  
85 assembly checkpoint function (Bass and Cortez, 2019). During meiotic prophase I,  
86 homologous chromosomes pair and undergo recombination, with regions of asynapsis  
87 being subjected to DDR-dependent transcriptional silencing. ATR, along with meiosis  
88 specific HORMA (Hop1, Rev7, and Mad2)- domain proteins, TOPBP1, and other factors,  
89 localizes to unsynapsed chromatin regions in leptotene- and zygotene-stage cells

90 (Fedoriw et al., 2015). At pachynema, the homologs are fully synapsed, at which point  
91 ATR localizes only to the unsynapsed axes and throughout the chromatin of the X and Y  
92 chromosomes, where it triggers a mechanism called meiotic sex chromosome inactivation  
93 (MSCI). MSCI is essential for successful meiotic progression through the silencing of toxic  
94 Y-linked genes and sequestration of DDR proteins away from autosomes (Abe et al.,  
95 2020; Royo et al., 2010; Turner, 2015). Central to MSCI is ATR-mediated phosphorylation  
96 of BRCA1 and H2AX on chromatin loops (Fukuda et al., 2012; Royo et al., 2013; Turner  
97 et al., 2004). Similarly, ATR mediates meiotic silencing of unsynapsed chromatin (MSUC)  
98 at autosomes that have failed to synapse properly (Turner, 2007, 2015). Beyond silencing,  
99 ATR has an essential role in promoting RAD51 and DMC1 loading to enable meiotic DSB  
100 repair (Pacheco et al., 2018; Widger et al., 2018). Previous work indicates that HUS1 and  
101 RAD9A are largely dispensable for meiotic ATR activation (Lyndaker et al., 2013a;  
102 Vasileva et al., 2013), raising the intriguing possibility that HUS1B- and RAD9B-  
103 containing alternative 9-1-1 complexes contribute to ATR activation during mammalian  
104 meiosis.

105 In addition to its checkpoint activation role, the 9A-1-1 complex also functions as a  
106 molecular scaffold for proteins in multiple DNA repair pathways. For example, the 9A-1-1  
107 complex participates in homologous recombination by interacting with the RAD51  
108 recombinase (Pandita et al., 2006) and EXO1 exonuclease (Karras et al., 2013; Ngo et  
109 al., 2014; Ngo and Lydall, 2015). Consistent with these observations from mitotic cells,  
110 RAD9A co-localizes with RAD51 on meiotic chromosome cores (Lyndaker et al., 2013a).  
111 In wild-type pachytene-stage cells, RAD51 foci are lost as DSBs are resolved, whereas

112 without *Hus1* RAD51 is retained on spermatocyte autosomes into late prophase I  
113 (Lyndaker et al., 2013a).

114 Loss of any canonical 9A-1-1 subunit in mice leads to embryonic lethality (Han et al.,  
115 2010; Hopkins et al., 2004; Weiss et al., 2000). In conditional knockout (CKO) models,  
116 loss of *Hus1* or *Rad9a* in the testis results in persistent DSBs during meiotic prophase  
117 leading to reduced testis size, decreased sperm count, and sub-fertility (Lyndaker et al.,  
118 2013a; Vasileva et al., 2013). Interestingly, localization of RAD1 and RAD9A to meiotic  
119 chromosome cores only partially overlaps, with RAD1 localizing to asynapsed  
120 chromosomes and along the entire X chromosome, and RAD9A in a more punctate  
121 pattern suggestive of DSB sites (Freire et al., 1998; Lyndaker et al., 2013a). Although  
122 RAD9A fails to localize properly in *Hus1*-deficient meiocytes, RAD1 localization to meiotic  
123 chromosome cores is largely HUS1-independent, supporting the idea that RAD1 can act  
124 outside of the canonical 9A-1-1 complex.

125 The HUS1 and RAD9A paralogs, HUS1B and RAD9B, are highly expressed in testis  
126 (Hang et al., 2002; Hopkins et al., 2004). Based on our previous results and the findings  
127 discussed above, we previously hypothesized that meiocytes contain alternative 9-1-1  
128 complexes, RAD9B-RAD1-HUS1 (9B-1-1) and RAD9B-RAD1-HUS1B (9B-1-1B)  
129 (Lyndaker et al., 2013b). Since RAD1 has no known paralogs, it is expected to be  
130 common to both canonical and alternative 9-1-1 complexes. In order to elucidate the roles  
131 of each of the 9-1-1 complexes in mammalian meiosis, we generated *Rad1* CKO mice in  
132 which *Rad1* was disrupted specifically in male spermatocytes. *Rad1* CKO mice exhibited  
133 reduced sperm count, reduced testis size and severe germ cell loss associated with DSB  
134 repair defects, consistent with previous studies of HUS1 and RAD9A. However, homolog

135 synapsis and MSCI, which were largely unaffected in *Hus1* or *Rad9a* CKO mice, were  
136 disrupted by *Rad1* loss. Whole testis-phosphoproteomic analyses further highlighted the  
137 importance of multiple 9-1-1 complexes in ATR-mediated processes such as meiotic  
138 silencing and cohesin regulation. This study highlights the importance of canonical and  
139 alternative 9-1-1 complexes during mammalian meiosis and establishes key roles for  
140 these DDR clamps in ATR activation, homolog synapsis and MSCI.

141 **RESULTS**

142 **Evolution and tissue-specific expression of 9-1-1 subunits.**

143 Human RAD9A and RAD9B share 45% identity, while HUS1 and HUS1B are 48%  
144 identical (Dufault et al., 2003; Hang et al., 2002). Inspection of genomic sequences  
145 revealed that *Rad9b* genes are present in the syntenic genomic region of all placental  
146 species analyzed, whereas *Rad9a* was likely lost in a few species, including wallaby, tree  
147 shrew and sloth (Figure 1A-1B). Phylogenetic analysis suggested that the duplication  
148 event generating *Rad9a* and *Rad9b* occurred prior to the evolution of bony fish ancestors  
149 (*D. rerio*), whereas the single exon *Hus1b* gene likely arose after a retrocopy duplication  
150 event later in evolution in mammals. Ortholog matrix and evolutionary tree analyses of  
151 placental mammals further showed that *Rad1* is highly conserved, with no identifiable  
152 paralog.

153 Human and mouse gene expression data indicate that the 9-1-1 paralogs are highly  
154 expressed in testes but no other tissues, hinting at a potential role for RAD9B and HUS1B  
155 in spermatogenesis (Figure 1-figure supplement 1A). To further define the cell type-  
156 specific expression patterns of the 9-1-1 subunits within the testes, we mined single-cell  
157 RNA sequencing data from wild-type adult mouse testis (Grive et al., 2019), comparing  
158 relative expression in spermatogonia, spermatocytes, and Sertoli cells. *Rad9b* expression  
159 was highest in spermatocytes as compared to spermatogonia and Sertoli cells (Figure  
160 1C). Similarly, *Rad1* and *Hus1b* expression were highest in spermatocytes (Figure 1C).  
161 Conversely, *Rad9a* and *Hus1* relative gene expression was highest in spermatogonia  
162 (Figure 1C). As expected, we found expression of *Atr* and meiotic silencing genes  
163 *Hormad1* and *Hormad2* to be significantly higher in spermatocytes than spermatogonia

164 or Sertoli cells. Spermatogonia also displayed relatively high levels of *Atr*, along with  
165 *Topbp1* and *Etaa1* (Figure 1C). Analysis of expression data from human testis similarly  
166 showed that *Hus1b* and *Rad9b* expression was highest in spermatocytes, whereas *Rad1*  
167 and *Rad9a* expression was highest in spermatogonia and *Hus1* expression was highest  
168 in early spermatids (Guo et al., 2018). Together these results suggest that the 9-1-  
169 1/TOPBP1/ATR and ETAA1/ATR signaling axes are expressed in pre-meiotic  
170 spermatogonia and suggest roles for alternative 9-1-1 complexes in male meiosis.

171 To further analyze the evolutionary relationships between 9-1-1 subunits, we  
172 performed evolutionary rate covariation (ERC) analysis, which assesses correlations in  
173 gene evolutionary history and can reveal functionally significant relationships (Clark et al.,  
174 2012; Wolfe and Clark, 2015). ERC analysis was performed between all of the 9-1-1  
175 subunits in a pairwise fashion across 33 mammalian species (Clark et al., 2012).  
176 Significant ERC values were identified between the RAD1, HUS1, and RAD9B subunits,  
177 supporting the notion that alternative 9-1-1 complexes assemble in germ cells (Figure  
178 2A). These findings are consistent with reports that RAD9B physically interacts with  
179 RAD1, HUS1, and HUS1B (Dufault et al., 2003), and similarly that HUS1B interacts with  
180 RAD1 (Hang et al., 2002), suggesting that the paralogs contribute to alternative 9-1-1  
181 complexes that include RAD9B-RAD1-HUS1 (9B-1-1) and RAD9B-HUS1-HUS1B (9B-1-  
182 1B) (Figure 2B).

183

184 **Testis-specific RAD1 loss leads to increased germ cell apoptosis and infertility.**

185 To determine how disrupting the subunit shared by all of the 9-1-1 complexes  
186 impacted meiosis, we created a *Rad1* CKO model by combining a conditional *Rad1* allele

187 (Wit et al., 2011) with *Stra8-Cre*, which drives CRE expression in spermatogonia (Sadate-  
188 Ngatchou et al., 2008). A similar approach was previously used to create *Hus1* CKO mice  
189 (Lyndaker et al., 2013a), also on the inbred 129Sv/Ev background, enabling direct  
190 comparison of results between the two models. Experimental *Rad1* CKO mice carried  
191 one *Rad1*<sup>fl/fl</sup> allele, one *Rad1*-null allele, and *Stra8-Cre* (*Rad1*<sup>-/fl</sup>; *Cre*<sup>+</sup>). Mice that carried  
192 a wild-type *Rad1* allele (*Rad1*<sup>+/fl</sup>; *Cre*<sup>+</sup>) or lacked *Stra8-Cre* (*Rad1*<sup>-/fl</sup>; *Cre*<sup>-</sup> or *Rad1*<sup>+/fl</sup>; *Cre*<sup>-</sup>  
193 ) were used as littermate controls. Both *Rad1* CKO and control mice were born at  
194 expected frequency.

195 Immunoblotting of whole testis lysates from 12-week-old *Rad1* CKO mice confirmed  
196 significant reduction in RAD1 protein (n=5 control and 5 CKO; Figure 2C). The residual  
197 RAD1 protein observed in *Rad1* CKO mice could arise from somatic cells of the testis or  
198 pre-meiotic germ cells. However, we cannot exclude the possibility that persistent RAD1  
199 protein exists in spermatocytes due to partial CRE recombinase efficacy or perdurance  
200 of RAD1 protein from pre-meiotic stages. Testes from *Rad1* CKO males were one-third  
201 the size of control testes at 4 weeks of age, while bodyweight was not altered (Figure 2D).  
202 Hematoxylin and eosin (H&E) staining of testis sections from control and *Rad1* CKO mice  
203 showed a reduction in tubule size starting at 4 weeks in CKO mice, with the phenotype  
204 being much more severe in 12-week-old mice (Figure 2D-E). Similar to previous findings  
205 in *Hus1* CKO males (Lyndaker et al., 2013a), *Rad1* CKO mice displayed increased  
206 apoptosis of zygotene/pachytene-staged cells (Figure 2F-G). In *Rad1* CKO mice, round  
207 spermatids were observed in some histology sections in 4-week-old and 12-week-old  
208 mice, possibly reflecting incomplete deletion and continued RAD1 expression in some  
209 meiocytes.

210 TUNEL staining confirmed significantly increased apoptosis in testes from *Rad1* CKO  
211 mice starting at 4 weeks of age (Figure 2F-G). 4-week-old *Rad1* CKO mice contained 2.4  
212  $\pm$  0.8 apoptotic nuclei per seminiferous tubule, compared to 0.5  $\pm$  0.4 in control mice.  
213 Apoptosis continued to be significantly elevated in 12-week-old *Rad1* CKO mice (2.0  $\pm$   
214 0.7 positive nuclei per tubule) as compared to control mice (0.6  $\pm$  0.4 positive nuclei per  
215 tubule) and was apparent in zygotene/pachytene-staged cells (Figure 2F-G). To quantify  
216 the impact of *Rad1* loss on germ cells, we stained testis sections for the germ cell-specific  
217 antigen TRA98 (Carmell et al., 2016). Tubules from control mice at 4 or 12 weeks of age  
218 contained an average of 220.2  $\pm$  26.3 or 254.3  $\pm$  45.5 TRA98-positive cells per tubule  
219 respectively (Figure 2-figure supplement 1A-B). However, in the absence of RAD1  
220 tubules contained only 74.89  $\pm$  7.5 TRA98-positive cells in 4-week-old mice and 47.8  $\pm$   
221 8.28 in 12-week-old males.

222 *Stra8-Cre* expression occurs as cells are committing to undergo meiosis (Sadate-  
223 Ngatchou et al., 2008). We therefore anticipated that the apoptosis and germ cell loss  
224 observed in *Rad1* CKO mice were due to meiotic defects. To address the possibility of  
225 pre-meiotic defects in *Rad1* CKO mice, we assessed mice at 8 days postpartum (dpp),  
226 prior to meiotic entry. H&E staining, along with TUNEL and TRA98 staining of sections  
227 from both control and *Rad1* CKO mice, showed no significant differences between  
228 genotypes at 8 dpp (Figure 2-figure supplement 1A-D). To further confirm that RAD1 loss  
229 did not affect cells prior to meiotic entry, we stained sections for LIN28, a marker of  
230 spermatogonial stem cells (SSCs), which have not initiated meiosis (Aeckerle et al.,  
231 2012). As expected, no significant differences in LIN28 staining were observed between  
232 genotypes in testes from mice at 8 dpp or 4 weeks of age (Figure 2-figure supplement

233 1C-D), consistent with the notion that RAD1 targeting is specific to meiotic cells. However,  
234 12-week-old *Rad1* CKO mice had a significant decrease in LIN28-positive cells when  
235 compared to control mice. This later loss of LIN28-positive cells in *Rad1* CKO mice can  
236 be attributed to the large-scale germ cell loss, which could indirectly disrupt the  
237 environment required for proper SSC proliferation and survival.

238 Next, we tested how localization of 9-1-1 subunits was affected by RAD1 loss.  
239 Consistent with prior results (Freire et al., 1998; Lyndaker et al., 2013a) RAD1 localized  
240 in control mice as foci on chromosome cores that were not yet synapsed during  
241 leptotema and zygonema, and was present on the core axis of the X and Y chromosomes  
242 in pachynema (Figure 3A). RAD1 expression was completely absent in 43% of  
243 spermatocytes from 12-week-old *Rad1* CKO mice, whereas 100% of control cells showed  
244 proper RAD1 localization and abundance in zygotene- and pachytene-stage cells (Figure  
245 3A). RAD1 expression in *Rad1* CKO meiocytes could be attributed to cells that failed to  
246 undergo CRE-mediated recombination or in which RAD1 levels were not yet fully  
247 depleted. The fact that *Rad1* CKO cells were prone to apoptosis would be expected to  
248 eliminate cells lacking RAD1, leaving RAD1-intact meiocytes enriched among the  
249 remaining cells. We next evaluated how RAD1 loss impacted RAD9A/B localization. In  
250 control samples, RAD9A and RAD9B localized to unsynapsed regions as foci in  
251 leptotene- and zygotene-staged cells (Figure 3B and Figure 3-figure supplement 1A). By  
252 pachynema, RAD9A and RAD9B localized primarily to the XY cores as foci. RAD9A and  
253 RAD9B localization were absent in 79% and 72%, respectively, of *Rad1* CKO meiotic  
254 spreads (Figure 3B and Figure 3-figure supplement 1A).

255 *Rad1* CKO mice had no epididymal sperm (Table 1). To assess if *Rad1* CKO mice  
256 were infertile, control and *Rad1* CKO mice were bred with wild-type females. Control mice  
257 bred with wild-type females yielded 10 pregnancies and 66 viable pups, whereas *Rad1*  
258 CKO mice had no viable offspring from 15 matings with wild-type females. Overall, these  
259 results indicate that RAD1 disruption severely compromised spermatogenesis and  
260 fertility. Moreover, the reduced testis weight and increased apoptosis in *Rad1* CKO mice  
261 were more severe than those in mice with *Hus1* or *Rad9a* loss (Lyndaker et al., 2013a;  
262 Vasileva et al., 2013), suggesting a broader role for RAD1 in meiocytes.

263

264 ***Rad1* loss results in synapsis defects and increased DNA damage.**

265 During meiosis, SC formation is critical for homologous chromosomes to pair and fully  
266 synapse (Zickler and Kleckner, 2015). Co-staining for the SC markers SYCP1 and  
267 SYCP3 revealed that  $59.5 \pm 4.3\%$  of meiocytes from *Rad1* CKO mice had whole  
268 chromosomes that remained unsynapsed and/or aberrant synapsis events involving  
269 multiple chromosomes, whereas 100% of meiocytes from control mice displayed normal  
270 homolog synapsis (Figure 3C and Figure 3-figure supplement 1C). RAD1 staining in  
271 meiocytes from 12-week-old *Rad1* CKO mice revealed that all cells that lacked RAD1  
272 displayed abnormal synapsis, with an average of only 8 chromosomes fully synapsed  
273 chromosomes per cell (Figure 3-figure supplement 1D). Cells with asynapsis that  
274 contained four or more synapsed homologous chromosomes were classified as  
275 pachytene-like cells, and subsequent analyses focused on this population of *Rad1* CKO  
276 meiocytes.

277 The  $\gamma$ H2AX staining pattern was similar in *Rad1* CKO and control spreads at  
278 leptonema and zygonema (Figure 3D). However, 97% of pachytene-like *Rad1* CKO cells  
279 showed  $\gamma$ H2AX present at asynaptic sites, with no clear presence of a sex body (n= 98  
280 cells, 3 CKO mice). Interestingly, a subset of asynaptic regions in *Rad1* CKO cells lacked  
281 detectable  $\gamma$ H2AX staining (Figure 3D, white arrow heads), suggesting that the DNA  
282 damage signaling at asynaptic sites was perturbed (Figure 3-figure supplement 1B).

283 Given that spermatocytes from *Rad1* CKO mice exhibited significantly increased  
284 asynapsis, we next assessed meiotic progression in these cells by staining for the histone  
285 variant H1T and the recombination marker MLH1. First, we questioned whether *Rad1*  
286 CKO cells were able to progress past mid-pachynema. Histone variant H1T is a marker  
287 of mid-pachynema and later staged wild-type spermatocytes (Barchi et al., 2005). Control  
288 cells demonstrate H1T staining as they progress into mid-pachynema (Figure 3-figure  
289 supplement 1E). However, H1T staining was absent in *Rad1* CKO meiocytes, indicating  
290 that the cells failed to progress past mid-pachynema (Figure 3-figure supplement 1E). By  
291 mid-pachynema, crossover sites are normally marked by MLH1 (Eaker et al., 2002).  
292 MLH1 was not detected in any *Rad1* CKO cells at the pachytene-like stage (Figure 3-  
293 figure supplement 1F), further suggesting that *Rad1* CKO meiocytes fail to progress  
294 beyond early/mid-pachynema. Together the observations of  $\gamma$ H2AX abnormalities and SC  
295 defects in *Rad1* CKO cells indicate important roles for 9-1-1 complexes in ensuring  
296 homologous chromosome synapsis and appropriate DDR signaling in response to  
297 asynapsis.

298

299 **DSB repair is compromised in *Rad1* CKO spermatocytes.**

300 Because testis-specific *Hus1* or *Rad9a* CKO results in persistent meiotic DSBs with  
301 delayed repair kinetics (Lyndaker et al., 2013a; Vasileva et al., 2013), we investigated  
302 how RAD1 loss impacts DSB repair. Following MRE11-RAD50-NBS1 (MRN)-mediated  
303 resection of SPO11-induced meiotic DSB, Meiosis-specific with OB domains (MEIOB)  
304 and RPA localize to the ssDNA overhangs prior to RAD51 and DMC1 loading (Hinch et  
305 al., 2020; Luo et al., 2013; Shi et al., 2019). In control spermatocytes, RPA and MEIOB  
306 foci are abundant in early prophase I and diminish as DSBs are repaired. *Rad1* CKO  
307 testes had on average 50 fewer RPA foci than controls in leptotene-stage cells ( $194 \pm 54$   
308 control;  $146 \pm 37$  CKO; Figure 4A-B). Intriguingly, RPA foci in *Rad1* CKO cells appeared  
309 larger than those in control cells. In the absence of RAD1, MEIOB focus formation on  
310 chromatin cores in leptotene-stage cells was also significantly decreased as compared to  
311 control cells ( $230 \pm 45$  control;  $126 \pm 37$  CKO; Figure 4C-D). In control spermatocytes,  
312 MEIOB and RPA levels on meiotic chromosome cores decreased as the cells progressed  
313 into pachynema ( $115 \pm 27$  control MEIOB;  $52 \pm 41$  control RPA), whereas *Rad1* CKO  
314 cells showed persistence of MEIOB and RPA staining ( $132 \pm 38$  CKO MEIOB;  $100 \pm 44$   
315 CKO RPA; Figure 4A-D).

316 During prophase I in wild-type spermatocytes, RAD51 and DMC1 displace MEIOB  
317 and RPA from the ssDNA overhangs and drive the subsequent steps of homology search  
318 and strand invasion (Hinch et al., 2020; Luo et al., 2013; Shi et al., 2019). The persistence  
319 of MEIOB and RPA foci in *Rad1* CKO spermatocytes suggested that RAD1 loss might  
320 perturb RAD51 loading. On average, leptotene-stage cells from control mice contained  
321  $195 \pm 29$  RAD51 foci, whereas *Rad1* CKO cells at the same stage had  $60 \pm 30$  RAD51  
322 foci (Figure 4E-F). RAD51 foci continued to be significantly lower in zygotene-stage *Rad1*

323 CKO meiocytes, which contained  $96 \pm 43$  RAD51 foci per cells as compared to  $146 \pm 31$   
324 in controls. In control samples, RAD51 foci levels decreased as cells progressed from  
325 zygonema to pachynema, reflecting the successful repair of DSBs. However, *Rad1* CKO  
326 spermatocytes retained relatively high levels of RAD51 foci in pachytene-like-stage cells  
327 ( $67 \pm 44$  RAD51 foci) as compared to control pachytene-stage meiocytes ( $10 \pm 4$  RAD51  
328 foci) (Figure 4F). These results for RAD51 localization in *Rad1* CKO spermatocytes  
329 differed from those in *Hus1* CKO mice, where RAD51 appeared normal in early prophase  
330 and then was aberrantly retained at a small number of sites in pachytene-stage cells  
331 (Lyndaker et al., 2013a). Together these results suggest that the 9-1-1 complexes are  
332 critical for proper DSB repair during mammalian meiosis and that absence of RAD1, or to  
333 a lesser extent HUS1, leaves persistent unrepaired DSBs.

334 The delayed loading of MEIOB, RPA and RAD51 observed in *Rad1*-deficient  
335 spermatocytes raised the possibility that DSB formation was impaired. To determine  
336 whether the defects were related to DSB formation or the subsequent repair steps, we  
337 treated *Rad1* CKO and control mice with 5 Gy ionizing radiation, harvested testes 1-hour  
338 post treatment, and quantified RPA and RAD51 focus formation in leptotene- and  
339 zygotene-stage cells. Since exogenously induced DSBs are repaired via meiotic  
340 processes in early stages of prophase I (Enguita-Marruedo et al., 2019), this approach  
341 allowed us to test whether the alterations in DSB markers in *Rad1* CKO cells were due to  
342 reduced DSB formation or a DSB repair defect. Upon DSB induction via irradiation,  
343 control mice showed the expected increase in RPA and RAD51 focus formation at early  
344 prophase I stages (Figure 4G-H, and Figure 4-figure supplement 1A-B). By contrast,  
345 irradiation did not induce increased focus formation by RPA or RAD51 in *Rad1* CKO

346 spermatocytes. These results suggest an intrinsic defect in meiotic DSB repair when the  
347 9-1-1 complexes are disabled.

348

349 **The localization of key components of the ATR axis is compromised in the absence**  
350 **of RAD1.**

351 ATR is a primary regulator of MSCI, which involves several DDR factors that are ATR  
352 substrates (Pacheco et al., 2018; Turner, 2007, 2015; Widger et al., 2018). Given that the  
353 canonical 9A-1-1 complex plays a central role in stimulating ATR activity in somatic cells,  
354 we sought to determine the effect of RAD1 loss on the localization of ATR and its  
355 substrates in meiocytes. ATR localizes to unsynapsed regions at early stages of prophase  
356 I, and by pachynema it is sequestered mainly at the XY body where it initiates MSCI (Abe  
357 et al., 2020; Turner, 2015). Cells from *Rad1* CKO mice with synapsis defects showed ATR  
358 localization only at a subset of unsynapsed regions (Figure 5A).

359 TOPBP1 is required for ATR activation following replication stress (Mordes et al.,  
360 2008) and interacts with ATR during meiosis to ensure that meiotic silencing is properly  
361 initiated (Ellnati et al., 2017; Jeon et al., 2019). In control meiocytes, TOPBP1 was  
362 observed as discrete foci on unsynapsed chromosome cores throughout leptotene and  
363 zygotene (Figure 5B). At pachynema, TOPBP1 was found exclusively along the  
364 unsynapsed regions of the X and Y and present as a faint cloud on XY chromosome  
365 loops. By contrast, in pachytene-like stage *Rad1* CKO cells, TOPBP1 localized to only a  
366 subset of asynaptic sites, failing to coat the entirety of unsynapsed chromosome cores,  
367 similar to the pattern observed for ATR. Although these findings may suggest a role for  
368 the 9-1-1 complexes in promoting ATR and TOPBP1 localization to unsynapsed

369 chromosomal regions, it remains possible that the extensive asynapsis in *Rad1* CKO mice  
370 causes an insufficiency in the available pool of silencing factors needed to localize to all  
371 synaptic sites (Mahadevaiah et al., 2008).

372 Localization of HORMA-domain proteins 1 and 2 (HORMAD1 and HORMAD2) at  
373 unsynapsed chromatin is important for meiotic silencing (Fukuda et al., 2010; Wojtasz et  
374 al., 2009). Furthermore, HORMAD1 plays an important role in ATR recruitment to  
375 unsynapsed sites (Fukuda et al., 2010; Shin et al., 2010). We next examined whether  
376 defective ATR localization in the absence of RAD1 was the result of HORMAD  
377 mislocalization. In control cells, HORMAD1 and HORMAD2 were observed during early  
378 prophase I at chromosomal regions that were not yet synapsed (Figure 5C-D). By mid-  
379 pachynema the HORMADs localized strictly at the unsynapsed regions of the XY, similar  
380 to the localization of ATR. Notably, RAD1 loss did not alter HORMAD1 or HORMAD2  
381 localization to unsynapsed regions. Furthermore, the HORMADs were observed to  
382 entirely coat unsynapsed chromosome regions in *Rad1* CKO cells, in contrast to the  
383 failure of ATR and TOPBP1 to localize to all unsynapsed sites.

384

385 **Phosphorylation of key ATR substrates is disrupted in *Rad1* CKO meiocytes.**

386 ATR phosphorylates HORMAD1 (S375) and HORMAD2 (S271) at synaptic regions  
387 (Fukuda et al., 2012; Royo et al., 2013). In control cells, HORMAD2 (S271)  
388 phosphorylation was observed on the X and Y chromosome cores in mid-pachytene-  
389 stage cells as expected (Figure 5E). However, in pachytene-like *Rad1* CKO cells,  
390 phosphorylated HORMAD2 was detected at only a subset of unsynapsed regions. That  
391 HORMAD2 localized properly in the absence of RAD1 but lacked phosphorylation at an

392 ATR-regulated site strongly suggests a requirement for 9-1-1 complexes in meiotic ATR  
393 signaling.

394 The best characterized ATR substrate in somatic cells is the transducer kinase CHK1.  
395 CHK1 has been proposed to play a role in meiotic DSB repair and is suggested to aide  
396 progression through prophase I by removal of DNA damage response proteins such as  
397  $\gamma$ H2AX from autosomes {Abe, 2018 #163; Fedoriw, 2015 #157; Pacheco, 2018 #126}. In  
398 wild-type cells, CHK1 phosphorylation (S317) occurs during leptotene and zygotene at  
399 unsynapsed chromosomes. During pachynema, pCHK1 (S317) is apparent as a cloud  
400 over the sex body, similar to  $\gamma$ H2AX and ATR (Figure 5F). Interestingly, in the *Rad1* CKO  
401 mutant, pCHK1 was absent at all stages of prophase I. By contrast, meiotic spreads from  
402 *Hus1* CKO mice showed normal patterns of CHK1 (S317) and HORMAD2 (S271)  
403 phosphorylation (Figure 5E-F). That meiotic CHK1 phosphorylation is normal in the  
404 absence of HUS1 but disrupted by RAD1 loss suggests that alternative 9-1-1 complexes  
405 play an important role in activating the transducer kinase CHK1 during meiotic prophase  
406 I.

407 The defects in ATR signaling observed in *Rad1* CKO mice suggested that disruption  
408 of 9-1-1 complexes might impair meiotic silencing. To test this possibility, we evaluated  
409 meiotic silencing via RNA fluorescent in situ hybridization (FISH) for the X-chromosome  
410 gene *Scm1/2* that should be silenced in early pachynema-stage cells (Royo et al., 2010).  
411 *Scm1/2* expression was detected in  $7.1 \pm 0.6\%$  of early pachytene control cells while *Rad1*  
412 CKO cells showed expression in  $28.9 \pm 3.2\%$  ( $p < 0.0001$ ; Figure 5G), indicating that  
413 meiotic silencing was disrupted by RAD1 loss. The analysis of *Scm1/2* expression focused  
414 on cells with normal homolog synapsis and excluded those with asynapsis, which could

415 underestimate the extent of the silencing defect upon RAD1 loss since some cells with  
416 normal synapsis in *Rad1* CKO mice retain RAD1 expression. Nevertheless, these data  
417 demonstrate the importance of alternative 9-1-1 complexes in ensuring that ATR-  
418 mediated MSCI occurs.

419

420 **Comprehensive profiling of protein phosphorylation in testes from *Rad1* CKO mice.**

421 Our findings that phosphorylation of key ATR substrates like HORMAD2 and CHK1  
422 was disrupted in *Rad1* CKO mice prompted us to more thoroughly characterize how  
423 RAD1 loss impacts meiotic signal transduction. Since the 9-1-1 complex is well-  
424 established to regulate ATR activation, we sought to identify phosphorylation events that  
425 were dependent on both the 9-1-1 complex and ATR. To accomplish this, we analyzed  
426 not only *Rad1* CKO testes but also those from wild-type C57BL/6 (B6) mice treated with  
427 the ATR inhibitor (ATRi) AZ20 (Sims et al., 2021). Wild-type B6 males received either  
428 chronic (3 doses of 50mg/kg over 3 days) or acute (single dose of 50mg/kg for 4 hrs) ATR  
429 inhibitor treatment. Whole testis lysates were subjected to phosphoproteomic analysis by  
430 mass spectrometry. The *Rad1* CKO samples featured cell type-specific disruption of  
431 RAD1, but the chronic nature of RAD1 depletion might lead to secondary alterations in  
432 the phosphoproteome of these cells. Though not cell-type specific, systemic ATR  
433 inhibition was acute, limiting secondary effects. The combined phosphoproteomic  
434 analysis of *Rad1* CKO and ATRi-treated testes allowed us to accurately identify meiotic  
435 phosphorylation events dependent on the combined actions of the 9-1-1 complexes and  
436 ATR (Figure 6A-B).

437 Principal component analysis showed tight clustering of three independent *Rad1* CKO  
438 samples and established that the *Rad1* CKO samples differed from ATRi samples along  
439 principal components 1 and 2 (Sims et al., 2021). High-quality phosphopeptides were  
440 designated after filtering for sites with a localization score >0.85 and considering only  
441 sites found in at least two independent experiment. Filtering of the data in this manner  
442 resulted in a total of 12,220 phosphopeptides. 863 phosphopeptides had significantly  
443 reduced phosphorylation in both *Rad1* CKO and ATRi samples relative to their matched  
444 controls and were considered to be RAD1- and ATR-dependent. 42 of these were  
445 differentially phosphorylated at S/T-Q sites, the ATR target motif (Blackford and Jackson,  
446 2017) (Figure 6B).

447 STRING-db was used to obtain gene ontologies (GO) for the differentially  
448 phosphorylated S/T-Q sites, and the top ten terms were highlighted in a chord diagram  
449 (Figure 6C). Major pathways known to be linked to ATR and the 9-1-1 complex were  
450 identified, with the top two terms being cellular response to DNA metabolic processes and  
451 DNA repair. The GO chord diagram further showed that nine of the terms included  
452 TOPBP1, and six of the terms included ATR. DDR proteins whose phosphorylation was  
453 dependent upon both RAD1 and ATR included proteins such as MDC1, involved in  
454 meiotic silencing, as well as DNA end-resection factors like CTIP and RAD50. The  
455 reduced phosphorylation of CTIP and RAD50 was notable in light of the observation that  
456 localization of the ssDNA binding proteins RPA and MEIOB, as well as the recombinase  
457 RAD51, was defective in *Rad1* CKO meiocytes, hinting at a potential role for the 9-1-1  
458 complexes in DSB processing.

459

460 **A role for 9-1-1 complexes in cohesin regulation**

461 Cohesins are critical for ensuring proper chromosome segregation in both mitotic and  
462 meiotic cells (Ishiguro, 2019). Loss of meiosis-specific cohesins, such as SMC1 $\beta$ , REC8  
463 or RAD21L, results in phenotypes that include DSB repair failure and synapsis defects  
464 (Challa et al., 2019; Ishiguro, 2019; Ward et al., 2016). SC assembly is also dependent  
465 upon proper cohesin loading (Eijpe et al., 2003; Llano et al., 2012). Interestingly,  
466 phosphorylation of SC components SYCP1 and SYCP2 was reduced in both *Rad1* CKO  
467 and ATRi-treated mice in the phosphoproteomic screen (Figure 6B-C). Cohesin complex  
468 components such as SMC3 and SMC1 $\beta$  also showed reduced phosphorylation in both  
469 ATRi and *Rad1* CKO samples. Furthermore, correlated evolutionary relationships, as  
470 measured by ERC analysis, were observed between genes encoding 9-1-1 subunits and  
471 those encoding cohesin and SC proteins, including SMC1 $\beta$ , RAD21L1, SYCP2, and  
472 SYCE1 (Figure 7A-B and Figure 7-figure supplement 1A-B). ERC network analysis of the  
473 relationship between proteins involved in meiosis I and the 9-1-1 subunits revealed a  
474 clustering of RAD9B, RAD1 and HUS1, while RAD9A and HUS1B did not show high ERC  
475 values with the other 9-1-1 subunits and had mostly separate network interactions (Figure  
476 7-figure supplement 1A-B). Both the ERC data and phosphoproteomic results implicate  
477 RAD1-containing 9-1-1 complexes in SC formation and cohesin during mammalian  
478 meiosis, consistent with the aberrant synapsis observed in *Rad1* CKO but not *Hus1* CKO  
479 spermatocytes.

480 SMC3 phosphorylation (pSMC3) was previously shown to be ATR-dependent  
481 throughout meiotic prophase (Fukuda et al., 2012). Co-staining for RAD1 and pSMC3  
482 (1083) in wild-type spermatocytes revealed co-localization of RAD1 and pSMC3 (1083)

483 at the XY in pachynema-stage cells (Figure 7C). In control meiocytes, SMC3 was  
484 observed on chromatin cores throughout prophase I and was phosphorylated specifically  
485 at unsynapsed chromatin cores during leptotene and zygotene, and at the unsynapsed  
486 regions of the XY in mid-pachynema (Figure 7D). Although total SMC3 loading was  
487 unaffected, *Rad1* CKO spermatocytes showed reduced accumulation of phosphorylated  
488 SMC3 (pSMC3 S1083) at unsynapsed chromatin regions in pachytene-like cells as  
489 compared to mid-pachytene-stage control cells. Moreover, western blot analysis of whole  
490 testis lysates confirmed that SMC3 phosphorylation (pSMC3 S1083) was significantly  
491 reduced in testes from *Rad1* CKO mice (Figure 7E). Unlike *Rad1* CKO spermatocytes,  
492 *Hus1* CKO cells had grossly normal pSMC3 (S1083) localization to the XY in pachytene-  
493 stage spermatocytes. Interestingly, chronic ATRi treatment caused a decrease in pSMC3  
494 (S1083) localization to X and Y chromatin loops and XY cores (Figure 7D). Similar to the  
495 results in *Rad1* CKO spermatocytes, pSMC3 (S1083) localization was perturbed in  
496 spermatocytes from ATRi-treated mice despite the fact that SMC3 localization to  
497 chromosome cores appeared normal, suggesting a specific defect in SMC3  
498 phosphorylation (Figure 7D top panel). Together these results suggest that 9-1-1  
499 complexes and ATR act in conjunction to regulate meiotic cohesin phosphorylation.  
500

501 **DISCUSSION**

502 Here we report that testis-specific RAD1 loss results in defective homolog  
503 asynapsis, compromised DSB repair, faulty ATR signaling, and impaired meiotic  
504 silencing. Previous analyses of the canonical 9A-1-1 complex in meiosis revealed that  
505 loss of *Hus1* or *Rad9a* leads to a small number of unrepaired DSBs that trigger germ cell  
506 death (Lyndaker et al., 2013a; Vasileva et al., 2013). Yet, homolog synapsis, ATR  
507 activation and meiotic silencing all are grossly normal in the absence of the canonical 9-  
508 1-1 subunits HUS1 and RAD9A. The expanded roles for RAD1 identified here are  
509 consistent with its ability to additionally interact with RAD9B and HUS1B, paralogs that  
510 evolved in higher organisms and are highly expressed in germ cells. Together, our results  
511 support the idea that alternative 9-1-1 complexes evolved to play essential roles in meiotic  
512 DSB repair, homolog synapsis, and MSCI.

513 In *Rad1* CKO spermatocytes, RAD51 loading onto meiotic chromosome cores was  
514 significantly reduced at leptotene and zygotene relative to controls. In control cells,  
515 DSB repair is concluding and RAD51 chromatin levels are low by mid-pachynema, but  
516 substantial RAD51 focus formation was still observed in pachytene-like *Rad1* CKO cells,  
517 suggesting major DSB repair defects. The meiotic DSB repair defects following RAD1  
518 loss are similar to those previously observed in *Atr* loss of function mouse models.  
519 Zygote-stage cells from a Seckel mouse model with disrupted ATR expression have  
520 decreased RAD51 and DMC1 loading (Pacheco et al., 2018), similar to that of  
521 spermatocytes lacking RAD1. Meiotic RAD51 focus formation did not increase further in  
522 *Rad1* CKO meiocytes after irradiation. These findings suggest that, similar to what is  
523 observed in *Atr*-defective spermatocytes (Pacheco et al., 2018; Widger et al., 2018), the

524 defects in RAD51 loading were not due to decreased numbers of SPO11-induced DSBs  
525 in *Rad1* CKO mice, highlighting an important role for the 9-1-1 complexes in the  
526 subsequent repair of meiotic DSBs.

527 Unlike what is observed in *Atr* mutants and ATR inhibitor-treated mice, localization of  
528 ssDNA markers MEIOB and RPA to meiotic cores was significantly reduced in the  
529 absence of RAD1. The 9-1-1 complex is well-established to modulate DNA end resection,  
530 having stimulatory or inhibitory effects in different contexts. In both yeast and mammals,  
531 the resection-stimulatory effects of the 9-1-1 complex involve recruitment of the Exo1 and  
532 Dna2 nucleases to DNA (Blaikley et al., 2014; Karras et al., 2013; Ngo et al., 2014; Ngo  
533 and Lydall, 2015). Our phosphoproteomic analysis of *Rad1* CKO testes and ATRi-treated  
534 mice also revealed a significant decrease in phosphorylation of proteins involved in DNA  
535 end resection, including RAD50, NBS1, and CTIP. Conditional *Nbs1* knockout in testes  
536 was previously reported to cause a decrease in chromatin loading of RPA, MEIOB and  
537 RAD51 (Zhang et al., 2020), similar to that in *Rad1* CKO mice, further suggesting potential  
538 functional interplay between the 9-1-1/ATR signaling axis and MRN complex during  
539 meiosis.

540 Somatic activation of ATR via 9A-1-1/TOPBP1 interaction is well established;  
541 however, ATR and TOPBP1 localization in spermatocytes was unperturbed in the  
542 absence of *Hus1*. ATR-dependent processes such as sex body formation and meiotic  
543 silencing still occurred without HUS1 and RAD9A (Lyndaker et al., 2013a; Vasileva et al.,  
544 2013). By contrast, the localization of ATR, TOPBP1 and BRCA1 to unsynapsed regions  
545 was compromised in *Rad1* CKO spermatocytes. ATR and BRCA1 work in a positive  
546 feedback loop to encourage meiotic silencing (Royo et al., 2013; Turner et al., 2004), and

547 the canonical and alternative 9-1-1 complexes may also be part of this regulatory circuitry.

548 Phosphorylation of some ATR targets, such as H2AX and HORMAD2, still occurred in

549 *Rad1* CKO spermatocytes but only at a subset of unsynapsed chromatin regions. It

550 should be noted that HORMAD1 and HORMAD2 localized appropriately to all

551 unsynapsed regions independently of RAD1, indicating that HORMAD localization was

552 not sufficient to driving ATR signaling and highlighting essential roles for the 9-1-1

553 complexes in meiotic ATR activation, possibly through interaction with TOPBP1. Other

554 ATR substrates were more profoundly affected by RAD1 loss. CHK1 phosphorylation

555 during meiosis was absent in *Rad1* CKO mice but present in *Hus1* CKO mice, suggesting

556 that HUS1-independent alternative 9-1-1 complexes are necessary for meiotic CHK1

557 activation. CHK1 is required for timely ATR localization to the XY at mid-pachynema and

558 MSCI initiation (Abe et al., 2018), and proper loading of RAD51 and DMC1 onto chromatin

559 depend on CHK1 phosphorylation by ATR (Pacheco et al., 2018). Thus, the CHK1

560 phosphorylation defects described here when all 9-1-1 complexes are disrupted could

561 contribute to multiple phenotypes observed in *Rad1* CKO spermatocytes, including

562 impaired silencing and faulty DSB repair.

563 We also observed reduced SC protein phosphorylation in *Rad1* CKO and ATRi-treated

564 mice, suggesting a role for the 9-1-1 complexes in mammalian SC formation. Studies in

565 *S. cerevisiae* show that direct interaction between the 9-1-1 complex and an SC

566 component, Red1, is required for both meiotic checkpoint signaling and SC formation

567 (Eichinger and Jentsch, 2010). Additionally, the budding yeast 9-1-1 complex also directly

568 interacts with Zip3, a member of the ZMM (Zip, Mer, Msh) group of proteins that promote

569 initiation of SC formation and crossover recombination. Notably, budding yeast 9-1-1 and

570 clamp loader mutants show reduced ZMM assembly on chromosomes, impaired SC  
571 formation, and reduced interhomolog recombination (Eichinger and Jentsch, 2010; Ho  
572 and Burgess, 2011; Shinohara et al., 2019; Shinohara et al., 2015).

573 ATR phosphorylates several cohesin complex components such as SMC1 $\beta$  and  
574 SMC3 (Fukuda et al., 2012). Phosphorylation of these proteins at the canonical ATR S/T-  
575 Q motif was downregulated in both ATRi-treated and *Rad1* CKO mice. SMC3 localization  
576 to meiotic chromosome cores was unperturbed, but SMC3 phosphorylation was  
577 dependent on RAD1 and ATR. It is important to note that additional proteins that are part  
578 of the cohesin complex, such as WAPL and SORORIN, also showed reduced  
579 phosphorylation in our phosphoproteomic screen. NIPBL, which functions in association  
580 with Mau2 as a SMC loader that localizes to chromosomal axes from zygonema to mid-  
581 pachynema (Visnes et al., 2014) also had reduced phosphorylation in testes from *Rad1*  
582 CKO and ATRi-treated mice. Interestingly, in *C. elegans*, SCC-2<sup>NIPBL</sup> loss disrupts DSB  
583 processing, cohesin loading and 9-1-1 recruitment to DNA damage sites (Lightfoot et al.,  
584 2011).

585 In addition to phosphoproteomics, we used ERC analysis to reveal potential  
586 mechanistic roles for 9-1-1 subunits. ERC analysis can infer functional protein partners  
587 based upon correlated rates of evolutionary change. Consistent with our  
588 phosphoproteomics data, this analysis highlighted significant evolutionary correlations  
589 between the genes encoding 9-1-1 complex subunits and those encoding proteins  
590 involved in SC formation, such as SYCP1, SYCE1, SYCE1L and SYCE2, in addition to  
591 RAD21, RAD21L and SMC1 $\beta$  which are involved in cohesion. Defects in homolog  
592 synapsis in *Rad1* CKO mice, together with the decreased cohesin phosphorylation,

593 further implicates the 9-1-1 complexes in these key aspects of meiotic chromosome  
594 structure. However, further exploration of the mechanisms underlying the interactions  
595 between SC proteins, cohesin, and the 9-1-1 complexes is necessary and may provide  
596 insights into the basis for the DSB repair defects in *Rad1* CKO mice, as proper SC  
597 formation and cohesin function is important for DSB repair (Ishiguro, 2019).

598 In mitotic cells, ATR activation is dependent on the 9-1-1/TOPBP1 axis under cellular  
599 stress, while ATR activation during unperturbed conditions relies on ETAA1 (Bass and  
600 Cortez, 2019). The potential contributions of ETAA1 to meiotic ATR activation have yet to  
601 be directly assessed. Our phosphoproteomic screen showed that RAD1-independent,  
602 ATR-dependent differentially phosphorylated proteins were associated with top gene  
603 ontology terms of cellular processes and organelle organization (Sims et al., 2021). Mice  
604 expressing a ETAA1 mutant with a 42 amino acid deletion show signs of replication stress  
605 but are fertile (Miosge et al., 2017). Understanding the differential roles of 9-1-1/TOPBP1  
606 and ETAA1 in meiotic ATR activation may highlight different modes of structure-specific  
607 ATR activation that are coupled with distinct downstream outputs.

608 Although this study highlights key meiotic functions of both canonical and alternative  
609 9-1-1 complexes, our approach does not resolve the relative importance of the DNA repair  
610 and checkpoint signaling roles of the 9-1-1 complexes during meiosis. Previous studies  
611 identified separable roles for 9-1-1 complexes in ATR activation via TOPBP1 interaction,  
612 and DNA repair protein scaffolding through the outer surface of 9-1-1 clamps (Lim et al.,  
613 2015). The loss of 9-1-1 complex formation and loading in *Rad1* CKO mice disrupts both  
614 of these roles. In budding yeast, the direct interactions between the 9-1-1 complex and  
615 Red1 as well as Zip3, together with additional evidence that the roles for 9-1-1 in SC

616 formation and recombination can be distinguished from those of Mec1 (ATR), provide  
617 compelling support for the notion that the 9-1-1 complex executes signaling-independent  
618 functions during meiosis, aside from its roles in checkpoint signaling (Eichinger and  
619 Jentsch, 2010; Shinohara et al., 2019; Shinohara et al., 2015). In the future, separation-  
620 of-function 9-1-1 mouse mutants could be used to clarify precisely how the 9-1-1  
621 complexes mediate meiotic processes such as homolog synapsis, cohesion, and  
622 silencing. Moreover, continued genetic and biochemical analysis of the paralogs RAD9B  
623 and HUS1B holds promise for resolving the differential and overlapping roles of the  
624 canonical and alternative 9-1-1 complexes in spermatogenesis.

625

626 **MATERIALS AND METHODS**

627

628 **Mice and genotyping**

629 *Rad1* CKO and control mice on the 129Sv/Ev background were generated by crossing  
630 *Rad1*<sup>fl/fl</sup> mice with *Rad1*<sup>+/+</sup>, *Stra8-Cre*<sup>+</sup> mice to generate *Rad1*<sup>+/fl</sup>, *Stra8-Cre*<sup>+</sup> (*Rad1*<sup>+/−</sup>,  
631 *Stra8-Cre*<sup>+</sup>) mice. *Stra8-Cre* mice containing one null *Rad1* allele (*Rad1*<sup>+/−</sup>, *Stra8-Cre*<sup>+</sup>)  
632 were crossed with *Rad1*<sup>fl/fl</sup> mice to generate experimental germ-cell specific *Rad1*  
633 conditional knockout mice (*Rad1*<sup>−/fl</sup>, *Stra8-Cre*<sup>+</sup>) and control mice (*Rad1*<sup>+/fl</sup>, *Stra8-Cre*<sup>+</sup>;  
634 *Rad1*<sup>+/fl</sup>, *Stra8-Cre*<sup>−</sup>; *Rad1*<sup>−/fl</sup>, *Stra8-Cre*<sup>−</sup>). *Rad1*<sup>fl/fl</sup> mice carry a conditional *Rad1* allele  
635 containing a K185R mutation that does not affect RAD1 function (Wit et al., 2011). *Hus1*  
636 conditional knockout mice were used as previously reported (Lyndaker et al., 2013a). All  
637 mice used for this study were handled following federal and institutional guidelines under  
638 a protocol approved by the Institutional Animal Care and Use Committee (IACUC) at  
639 Cornell University. The key resources table lists the genotyping primers used in this study.

640

641 **Fertility tests**

642 For fertility testing, 8- to 12-week-old *Rad1*<sup>−/fl</sup>, *Stra8-Cre*<sup>+</sup> and control males were singly  
643 housed with wild-type FVB females, where copulatory plugs were monitored daily. Once  
644 a plugged female was detected the female was removed to a separate cage and  
645 monitored for pregnancy. Viable pups were counted on the first day of life.

646

647 **Epididymal sperm counts**

648 Both caudal epididymides from 12-week-old mice were minced with fine forceps in 37°C  
649 in a petri dish containing 1x Phosphate Buffered Saline (PBS) and fixed in 10% neutral-  
650 buffered formalin (1:25 dilution). Sperm were counted using a hemacytometer and  
651 analyzed statistically using a Student's t-test between control and *Rad1* CKO mice.

652

### 653 **Irradiation of mice**

654 Control and *Rad1* CKO mice were placed in a <sup>137</sup>Cesium sealed source irradiator (J.L.  
655 Shepherd and Associates) with a rotating turntable and irradiated with 5Gy IR. Testes  
656 were harvested for meiotic spreads 1-hour post radiation.

657

### 658 **Immunoblotting**

659 Whole testis lysates from *Rad1* CKO, *Hus1* CKO, and control mice were prepared in RIPA  
660 buffer (10mM Tris-HCl, pH 8.0, 1mM EDTA, 0.5mM EGTA, 1% Triton X-100, 0.1% Sodium  
661 Deoxycholate, 0.1% SDS, 140mM NaCl) supplemented with aprotinin, leupeptin, sodium  
662 orthovanadate, and phenyl-methylsulfonyl fluoride. Cell lysates were resolved by SDS-  
663 PAGE and immunoblotted using standard procedures. Bands were visualized on a  
664 VersaDoc MP 5000 Model (Bio-Rad) using a 1:1 ratio of WesternBright ECL  
665 Luminol/enhancer solution to WesternBright Peroxide Chemiluminescent peroxide  
666 solution (Advansta). Antibody information is provided in key resources table.

667

### 668 **Histology and immunohistochemistry**

669 Testes were harvested from mice aged to 8dpp, 4 weeks or 12 weeks of age. Testes were  
670 then fixed overnight in either Bouin's (Ricca chemicals) for hematoxylin and eosin staining

671 or 10% neutral-buffered formalin (Fisher) for LIN28, TRA98, and TUNEL staining. Fixed  
672 testes were embedded in paraffin wax and sectioned at 5 $\mu$ m. Immunofluorescence  
673 staining was used to detect LIN28 using rabbit polyclonal anti-LIN28 antibody (Abcam,  
674 ab63740). Immunohistochemistry staining was used to detect TRA98 using rat  
675 monoclonal anti-TRA98 antibody (BioAcademia, 73-003). TUNEL assay was performed  
676 using the Apoptag® kit (EMD Millipore) as per the manufacturer's instructions. LIN28,  
677 TRA98 and TUNEL data were quantified in ImageJ by counting the number of positive  
678 cells per tubule for 50 tubules of each genotype for each age group. Differences between  
679 controls and *Rad1* CKOs was analyzed using Welch's unpaired t-test using Graphpad.  
680

#### 681 **Meiotic spreading and immunofluorescence staining**

682 Meiotic spreads were prepared from 8- to 12-week-old mice as previously described  
683 (Kolas et al., 2005). Briefly, tubules from mice were incubated on ice in hypotonic  
684 extraction buffer for 1 hour. Tubules were then minced into single cell suspension in  
685 100mM sucrose, and cells were spread on slides coated with 1% PFA with 0.15%  
686 TritonX-100 and incubated in a humidifying chamber for 4 hours or overnight. For  
687 immunostaining, slides were blocked using 10% goat serum and 3% BSA, followed by  
688 incubation overnight with primary antibody (listed in key resources table) at room  
689 temperature in a humidifying chamber. Secondary antibodies were incubated at 37°C for  
690 2 hours in the dark, and slides were then cover-slipped using anti-fade mounting medium  
691 (2.3% DABCO, 20mM Tris pH 8.0, 8 $\mu$ g DAPI in 90% glycerol). Meiotic chromosomal  
692 spreads were imaged with an AxioCam MRM using a Zeiss Imager Z1 microscope (Carl  
693 Zeiss, Inc.) and processed with ZEN Software (version 2.0.0.0;Carl Zeiss, Inc.).

694 Quantification of meiotic spreads was performed using Fiji for ImageJ. Statistical analysis  
695 was performed using Welch's unpaired t-test using Graphpad Prism8.

696

697 **RNA Fluorescence In-Situ Hybridization (RNA-FISH) and immunofluorescence**  
698 **Staining**

699 RNA FISH was carried out with digoxigenin labelled probe using BAC DNA, *Scml2*: RP24-  
700 204O18 (CHORI) and immunofluorescence using rabbit HORMAD2, antibody (gift from  
701 gift from A. Toth) as previously described (Mahadevaiah et al., 2009). Images of RNA  
702 FISH with immunofluorescence were captured using Deltavision Microscopy System  
703 (100x/1.35NA Olympus UPlanApo oil immersion objective).

704

705 **ATR inhibitor treatment of mice**

706 Wild-type B6 mice were treated via oral gavage with AZ20 (Selleck Chemicals)  
707 reconstituted in 10% DMSO (Sigma), 40% Propylene glycol (Sigma), and 50% water.  
708 Three different ATRi treatments were used. Chronic ATR inhibitor treatment was  
709 performed by treating mice daily for 3 days with 50mg/kg AZ20 and collecting 24 hours  
710 after final dose, or by treating with 2 doses of 50mg/kg AZ20 on the first 2 days and 1  
711 final dose of 25mg/kg AZ20 and collecting 4 hours after the final dose . Acute ATR  
712 inhibitor-treated mice were collected 4 hours after one dose of 50mg/kg AZ20.

713

714 **Phosphoproteomic analysis**

715 Whole testis lysates from 8-week-old AZ20 (ATRi) treated wild-type C57BL/6 and 12-  
716 week-old *Rad1* CKO mice were subjected to phosphopeptide enrichment and 6-plex TMT

717 (ThermoFisher) labeling (Sims et al., 2021). To identify differentially regulated  
718 phosphosites we performed a bow tie analysis as described in Sims et al. (Sims et al.,  
719 2021). Gene ontology enrichment with Benjamini-Hochberg adjustment to account for  
720 multiple hypothesis testing was done using STRINGdb. Terms were ranked based on their  
721 FDR values, and the top 10 gene ontology terms from the Biological Processes  
722 subontology were plotted using R package GOplot.

723

#### 724 **Orthology analysis**

725 Human 9-1-1 subunit sequences were used to obtain their respective orthologs from  
726 Ensemble 101(2020) and/or NCBI Gene from 33 representative mammalian species.  
727 Orthologs found in Ensemble having a  $\geq 50\%$  of both target and query sequence identity  
728 and a pairwise whole genome alignment score of  $\geq 50$  were considered to have high  
729 confidence. Orthologs that did not meet those criteria were considered to have low  
730 confidence. Sequences only found in NCBI Gene database were considered as high  
731 confidence if they were found to be syntenic. Synteny was determined based on whether  
732 the gene had at least one shared neighbor gene upstream or downstream that also was  
733 conserved. Species divergence across time was obtained from TimeTree website  
734 ([www.timetree.org](http://www.timetree.org)).

735

#### 736 **Phylogenetic analysis**

737 Protein sequences of 9-1-1 orthologs were obtained using NCBI HomoloGene. Multiple  
738 alignment of protein sequences was done using Clustal Omega (1.2.2) implemented in  
739 Geneious Prime (2020.0.5). A substitution model was tested using ProtTest (v. 3.4.2). The

740 selected substitution model with specific improvements was JTT+I+G+F (Jones-Taylor-  
741 Thornton; +I: invariable sites; +G: rate heterogeneity among sites; +F: observed amino  
742 acid frequencies). Improvements were included to take account for any evolutionary  
743 limitations due to conservation of protein structure and function. A nonrooted phylogenetic  
744 tree was made using Maximum Likelihood interference (4 gamma distributed rate)  
745 (Nguyen et al., 2015) and implemented with iTOL ([itol.embl.de](http://itol.embl.de)) (Letunic and Bork, 2019).  
746 Branch distance represents substitution rate and branch support was performed with  
747 1000 ultrafast bootstrap replicates. Nodes below 70% branch support were collapsed.

748

#### 749 **ERC analysis**

750 ERC calculations were completed using the Evolutionary Rate Covariation (ERC) web  
751 tool at [https://csb.pitt.edu/erc\\_analysis/](https://csb.pitt.edu/erc_analysis/) (Wolfe and Clark, 2015). Group analysis was  
752 performed to examine ERC values between all gene pairs indicated in Figure 2A , 7A and  
753 7B using UCSC gene sequences from 33 mammalian species as described in Priedigkeit  
754 et al. (Priedigkeit et al., 2015). For figure 7-figure supplement 1A and 1B, the protein set  
755 list for Gene Ontology subontology Meiosis I (GO:0007127) was obtained from AmiGO 2  
756 (v2.5.13). ERC values were calculated against each of the 9-1-1 subunits using the ERC  
757 analysis web site. Using R (v4.0.3) ERC values were depicted as a heatmap and a  
758 network plotted using the packages pheatmap (v1.0.12) and qgraph (v1.6.5) respectively.  
759 A cutoff of ERC value of 0.4 was used to determine significant comparisons. The  
760 Fruchterman & Reingold algorithm was used to generate a forced-directed layout to help  
761 determine clusters of highly connected nodes and after 500 iterations the distance  
762 between nodes shows absolute edge weight (ERC values) between nodes.

763 **COMPETING INTEREST STATEMENT**

764 The authors declare no competing financial interests.

765 **ACKNOWLEDGMENTS**

766 We are thankful to Dan Barbash and Eric Alani for helpful discussions and for providing  
767 critical feedback on the manuscript, to Mary Ann Handel and Attila Toth for providing  
768 reagents used in this study, and to Christina Jeon for early-stage contributions to the  
769 analysis of 9-1-1 subunit evolution. This work was supported in part by NIH grants R03  
770 HD083621 (to RSW), R01 HD095296 (to MBS and RSW), R01 HD097987 (to PEC), NSF  
771 predoctoral fellowship DGE-1144153 (to CP), and a National Center for Research  
772 Resources instrumentation grant (S10 RR023781). This work additionally was supported  
773 by European Research Council (CoG 647971) and the Francis Crick Institute, which  
774 receives its core funding from Cancer Research UK (FC001193), UK Medical Research  
775 Council (FC001193) and Wellcome Trust (FC001193).

776

777 **AUTHOR CONTRIBUTIONS**

778 Conceptualization: CP, AML, MAB-E, PEC, MBS, RSW; Methodology and  
779 experimentation: CP, GAAM, MAB-E, MG, MSD, EK, KJG, SKM, CT, CJS, JS; Data  
780 curation and analysis: CP, GAAM, VMF, MG, MSD, SKM, CT, CJS, JS; Project  
781 administration and funding: JMAT, PEC, MBS, RSW; Resources: NW, HJ, NLC, PEC, RF;  
782 Supervision: JMAT, PEC, MBS, RSW; Writing and editing: CP, GAAM, AML, JS, MAB-E,  
783 PEC, MBS, RSW.

784

785 **REFERENCES**

786 Abe, H., Alavattam, K.G., Hu, Y.C., Pang, Q., Andreassen, P.R., Hegde, R.S., and  
787 Namekawa, S.H. (2020). The Initiation of Meiotic Sex Chromosome Inactivation  
788 Sequesters DNA Damage Signaling from Autosomes in Mouse Spermatogenesis. *Curr  
789 Biol* 30, 408-420 e405.

790 Abe, H., Alavattam, K.G., Kato, Y., Castrillon, D.H., Pang, Q., Andreassen, P.R., and  
791 Namekawa, S.H. (2018). CHEK1 coordinates DNA damage signaling and meiotic  
792 progression in the male germline of mice. *Human Molecular Genetics* 27, 1136-1149.

793 Aeckerle, N., Eildermann, K., Drummer, C., Ehmcke, J., Schweyer, S., Lerchl, A.,  
794 Bergmann, M., Kliesch, S., Gromoll, J., Schlatt, S., *et al.* (2012). The pluripotency factor  
795 LIN28 in monkey and human testes: a marker for spermatogonial stem cells? *Mol Hum  
796 Reprod* 18, 477-488.

797 Barchi, M., Mahadevaiah, S., Di Giacomo, M., Baudat, F., de Rooij, D.G., Burgoyne, P.S.,  
798 Jasin, M., and Keeney, S. (2005). Surveillance of different recombination defects in  
799 mouse spermatocytes yields distinct responses despite elimination at an identical  
800 developmental stage. *Mol Cell Biol* 25, 7203-7215.

801 Bass, T.E., and Cortez, D. (2019). Quantitative phosphoproteomics reveals mitotic  
802 function of the ATR activator ETAA1. *J Cell Biol* 218, 1235-1249.

803 Bass, T.E., Luzwick, J.W., Kavanaugh, G., Carroll, C., Dungrawala, H., Glick, G.G.,  
804 Feldkamp, M.D., Putney, R., Chazin, W.J., and Cortez, D. (2016). ETAA1 acts at stalled  
805 replication forks to maintain genome integrity. *Nat Cell Biol* 18, 1185-1195.

806 Bhat, K.P., and Cortez, D. (2018). RPA and RAD51: fork reversal, fork protection, and  
807 genome stability. *Nat Struct Mol Biol* 25, 446-453.

808 Blackford, A.N., and Jackson, S.P. (2017). ATM, ATR, and DNA-PK: The Trinity at the  
809 Heart of the DNA Damage Response. *Mol Cell* 66, 801-817.

810 Blaikley, E.J., Tinline-Purvis, H., Kasperek, T.R., Marguerat, S., Sarkar, S., Hulme, L.,  
811 Hussey, S., Wee, B.Y., Deegan, R.S., Walker, C.A., *et al.* (2014). The DNA damage  
812 checkpoint pathway promotes extensive resection and nucleotide synthesis to facilitate  
813 homologous recombination repair and genome stability in fission yeast. *Nucleic Acids  
814 Res* 42, 5644-5656.

815 Bolcun-Filas, E., and Handel, M.A. (2018). Meiosis: the chromosomal foundation of  
816 reproduction. *Biol Reprod* 99, 112-126.

817 Cahoon, C.K., and Hawley, R.S. (2016). Regulating the construction and demolition of  
818 the synaptonemal complex. *Nat Struct Mol Biol* 23, 369-377.

819 Carmell, M.A., Dokshin, G.A., Skaletsky, H., Hu, Y.C., van Wolfswinkel, J.C., Igarashi,  
820 K.J., Bellott, D.W., Nefedov, M., Reddien, P.W., Enders, G.C., *et al.* (2016). A widely  
821 employed germ cell marker is an ancient disordered protein with reproductive functions  
822 in diverse eukaryotes. *Elife* 5.

823 Challa, K., Shinohara, M., and Shinohara, A. (2019). Meiotic prophase-like pathway for  
824 cleavage-independent removal of cohesin for chromosome morphogenesis. *Curr Genet*  
825 65, 817-827.

826 Clark, N.L., Alani, E., and Aquadro, C.F. (2012). Evolutionary rate covariation reveals  
827 shared functionality and coexpression of genes. *Genome Res* 22, 714-720.

828 Cotta-Ramusino, C., McDonald, E.R., Hurov, K., Sowa, M.E., Harper, J.W., and Elledge,  
829 S.J. (2011). A DNA Damage Response Screen Identifies RHINO, a 9-1-1 and TopBP1  
830 Interacting Protein Required for ATR Signaling. *Science* 332, 1313-1317.

831 Delacroix, S., Wagner, J.M., Kobayashi, M., Yamamoto, K., and Karnitz, L.M. (2007). The  
832 Rad9-Hus1-Rad1 (9-1-1) clamp activates checkpoint signaling via TopBP1. *Genes Dev*  
833 21, 1472-1477.

834 Dufault, V.M., Oestreich, A.J., Vroman, B.T., and Karnitz, L.M. (2003). Identification and  
835 characterization of RAD9B, a paralog of the RAD9 checkpoint gene. *Genomics* 82, 644-  
836 651.

837 Eaker, S., Cobb, J., Pyle, A., and Handel, M.A. (2002). Meiotic prophase abnormalities  
838 and metaphase cell death in MLH1-deficient mouse spermatocytes: insights into  
839 regulation of spermatogenic progress. *Dev Biol* 249, 85-95.

840 Eichinger, C.S., and Jentsch, S. (2010). Synaptonemal complex formation and meiotic  
841 checkpoint signaling are linked to the lateral element protein Red1. *Proc Natl Acad Sci U*  
842 *S A* 107, 11370-11375.

843 Eichinger, C.S., and Jentsch, S. (2011). 9-1-1: PCNA's specialized cousin. *Trends*  
844 *Biochem Sci* 36, 563-568.

845 Eijpe, M., Offenberg, H., Jessberger, R., Revenkova, E., and Heyting, C. (2003). Meiotic  
846 cohesin REC8 marks the axial elements of rat synaptonemal complexes before cohesins  
847 SMC1beta and SMC3. *J Cell Biol* 160, 657-670.

848 Ellnati, E., Russell, H.R., Ojarikre, O.A., Sangrithi, M., Hirota, T., de Rooij, D.G.,  
849 McKinnon, P.J., and Turner, J.M.A. (2017). DNA damage response protein TOPBP1  
850 regulates X chromosome silencing in the mammalian germ line. *Proc Natl Acad Sci U S*  
851 *A* 114, 12536-12541.

852 Enguita-Marruedo, A., Martin-Ruiz, M., Garcia, E., Gil-Fernandez, A., Parra, M.T., Viera,  
853 A., Rufas, J.S., and Page, J. (2019). Transition from a meiotic to a somatic-like DNA

854 damage response during the pachytene stage in mouse meiosis. PLoS Genet 15,  
855 e1007439.

856 Fedoriw, A.M., Menon, D., Kim, Y., Mu, W., and Magnuson, T. (2015). Key mediators of  
857 somatic ATR signaling localize to unpaired chromosomes in spermatocytes.  
858 Development 142, 2972-2980.

859 Feng, S., Zhao, Y., Xu, Y., Ning, S., Huo, W., Hou, M., Gao, G., Ji, J., Guo, R., and Xu,  
860 D. (2016). Ewing Tumor-associated Antigen 1 Interacts with Replication Protein A to  
861 Promote Restart of Stalled Replication Forks. J Biol Chem 291, 21956-21962.

862 Fernandez-Capetillo, O., Mahadevaiah, S.K., Celeste, A., Romanienko, P.J., Camerini-  
863 Otero, R.D., Bonner, W.M., Manova, K., Burgoyne, P., and Nussenzweig, A. (2003).  
864 H2AX is required for chromatin remodeling and inactivation of sex chromosomes in male  
865 mouse meiosis. Dev Cell 4, 497-508.

866 Freire, R., Murguia, J.R., Tarsounas, M., Lowndes, N.F., Moens, P.B., and Jackson, S.P.  
867 (1998). Human and mouse homologs of *Schizosaccharomyces pombe* rad1(+) and  
868 *Saccharomyces cerevisiae* RAD17: linkage to checkpoint control and mammalian  
869 meiosis. Genes Dev 12, 2560-2573.

870 Fukuda, T., Daniel, K., Wojtasz, L., Toth, A., and Hoog, C. (2010). A novel mammalian  
871 HORMA domain-containing protein, HORMAD1, preferentially associates with  
872 unsynapsed meiotic chromosomes. Exp Cell Res 316, 158-171.

873 Fukuda, T., Pratto, F., Schimenti, J.C., Turner, J.M., Camerini-Otero, R.D., and Hoog, C.  
874 (2012). Phosphorylation of chromosome core components may serve as axis marks for  
875 the status of chromosomal events during mammalian meiosis. PLoS Genet 8, e1002485.

876 Gray, S., and Cohen, P.E. (2016). Control of Meiotic Crossovers: From Double-Strand  
877 Break Formation to Designation. *Annu Rev Genet* 50, 175-210.

878 Grive, K.J., Hu, Y., Shu, E., Grimson, A., Elemento, O., Grenier, J.K., and Cohen, P.E.  
879 (2019). Dynamic transcriptome profiles within spermatogonial and spermatocyte  
880 populations during postnatal testis maturation revealed by single-cell sequencing. *PLoS*  
881 *Genet* 15, e1007810.

882 Guo, J., Grow, E.J., Mlcochova, H., Maher, G.J., Lindskog, C., Nie, X., Guo, Y., Takei, Y.,  
883 Yun, J., Cai, L., *et al.* (2018). The adult human testis transcriptional cell atlas. *Cell Res*  
884 28, 1141-1157.

885 Haahr, P., Hoffmann, S., Tollenaere, M.A., Ho, T., Toledo, L.I., Mann, M., Bekker-Jensen,  
886 S., Raschle, M., and Mailand, N. (2016). Activation of the ATR kinase by the RPA-binding  
887 protein ETAA1. *Nat Cell Biol* 18, 1196-1207.

888 Han, L., Hu, Z., Liu, Y., Wang, X., Hopkins, K.M., Lieberman, H.B., and Hang, H. (2010).  
889 Mouse Rad1 deletion enhances susceptibility for skin tumor development. *Mol Cancer* 9,  
890 67.

891 Hang, H., Zhang, Y., Dunbrack, R.L., Jr., Wang, C., and Lieberman, H.B. (2002).  
892 Identification and characterization of a paralog of human cell cycle checkpoint gene  
893 HUS1. *Genomics* 79, 487-492.

894 Hinch, A.G., Becker, P.W., Li, T., Moralli, D., Zhang, G., Bycroft, C., Green, C., Keeney,  
895 S., Shi, Q., Davies, B., *et al.* (2020). The Configuration of RPA, RAD51, and DMC1  
896 Binding in Meiosis Reveals the Nature of Critical Recombination Intermediates. *Mol Cell*  
897 79, 689-701 e610.

898 Ho, H.C., and Burgess, S.M. (2011). Pch2 acts through Xrs2 and Tel1/ATM to modulate  
899 interhomolog bias and checkpoint function during meiosis. *PLoS Genet* 7, e1002351.

900 Hopkins, K.M., Auerbach, W., Wang, X.Y., Hande, M.P., Hang, H., Wolgemuth, D.J.,  
901 Joyner, A.L., and Lieberman, H.B. (2004). Deletion of mouse rad9 causes abnormal  
902 cellular responses to DNA damage, genomic instability, and embryonic lethality. *Mol Cell  
903 Biol* 24, 7235-7248.

904 Hopkins, K.M., Wang, X., Berlin, A., Hang, H., Thaker, H.M., and Lieberman, H.B. (2003).  
905 Expression of mammalian paralogues of HRAD9 and Mrad9 checkpoint control genes in  
906 normal and cancerous testicular tissue. *Cancer Res* 63, 5291-5298.

907 Inselman, A., Eaker, S., and Handel, M.A. (2003). Temporal expression of cell cycle-  
908 related proteins during spermatogenesis: establishing a timeline for onset of the meiotic  
909 divisions. *Cytogenet Genome Res* 103, 277-284.

910 Ishiguro, K.I. (2019). The cohesin complex in mammalian meiosis. *Genes Cells* 24, 6-30.

911 Jeon, Y., Park, M.K., Kim, S.M., Bae, J.S., Lee, C.W., and Lee, H. (2019). TopBP1  
912 deficiency impairs the localization of proteins involved in early recombination and results  
913 in meiotic chromosome defects during spermatogenesis. *Biochem Biophys Res Commun  
914* 508, 722-728.

915 Karras, G.I., Fumasoni, M., Sienski, G., Vanoli, F., Branzei, D., and Jentsch, S. (2013).  
916 Noncanonical role of the 9-1-1 clamp in the error-free DNA damage tolerance pathway.  
917 *Mol Cell* 49, 536-546.

918 Kolas, N.K., Svetlanov, A., Lenzi, M.L., Macaluso, F.P., Lipkin, S.M., Liskay, R.M.,  
919 Greally, J., Edelmann, W., and Cohen, P.E. (2005). Localization of MMR proteins on

920 meiotic chromosomes in mice indicates distinct functions during prophase I. *J Cell Biol*  
921 171, 447-458.

922 Lee, Y.C., Zhou, Q., Chen, J., and Yuan, J. (2016). RPA-Binding Protein ETAA1 Is an  
923 ATR Activator Involved in DNA Replication Stress Response. *Curr Biol* 26, 3257-3268.

924 Leloup, C., Hopkins, K.M., Wang, X., Zhu, A., Wolgemuth, D.J., and Lieberman, H.B.  
925 (2010). Mouse Rad9b is essential for embryonic development and promotes resistance  
926 to DNA damage. *Dev Dyn* 239, 2837-2850.

927 Letunic, I., and Bork, P. (2019). Interactive Tree Of Life (iTOL) v4: recent updates and  
928 new developments. *Nucleic Acids Res* 47, W256-W259.

929 Lightfoot, J., Testori, S., Barroso, C., and Martinez-Perez, E. (2011). Loading of meiotic  
930 cohesin by SCC-2 is required for early processing of DSBs and for the DNA damage  
931 checkpoint. *Curr Biol* 21, 1421-1430.

932 Lim, P.X., Patel, D.R., Poisson, K.E., Basuita, M., Tsai, C., Lyndaker, A.M., Hwang, B.J.,  
933 Lu, A.L., and Weiss, R.S. (2015). Genome Protection by the 9-1-1 Complex Subunit  
934 HUS1 Requires Clamp Formation, DNA Contacts, and ATR Signaling-independent  
935 Effector Functions. *J Biol Chem* 290, 14826-14840.

936 Lindsey-Boltz, L.A., Kemp, M.G., Capp, C., and Sancar, A. (2015). RHINO forms a  
937 stoichiometric complex with the 9-1-1 checkpoint clamp and mediates ATR-Chk1  
938 signaling. *Cell Cycle* 14, 99-108.

939 Llano, E., Herran, Y., Garcia-Tunon, I., Gutierrez-Caballero, C., de Alava, E., Barbero,  
940 J.L., Schimenti, J., de Rooij, D.G., Sanchez-Martin, M., and Pendas, A.M. (2012). Meiotic  
941 cohesin complexes are essential for the formation of the axial element in mice. *J Cell Biol*  
942 197, 877-885.

943 Luo, M., Yang, F., Leu, N.A., Landaiche, J., Handel, M.A., Benavente, R., La Salle, S.,  
944 and Wang, P.J. (2013). MEIOB exhibits single-stranded DNA-binding and exonuclease  
945 activities and is essential for meiotic recombination. *Nat Commun* 4, 2788.

946 Lyndaker, A.M., Lim, P.X., Mleczko, J.M., Diggins, C.E., Holloway, J.K., Holmes, R.J.,  
947 Kan, R., Schlafer, D.H., Freire, R., Cohen, P.E., *et al.* (2013a). Conditional inactivation of  
948 the DNA damage response gene Hus1 in mouse testis reveals separable roles for  
949 components of the RAD9-RAD1-HUS1 complex in meiotic chromosome maintenance.  
950 *PLoS Genet* 9, e1003320.

951 Lyndaker, A.M., Vasileva, A., Wolgemuth, D.J., Weiss, R.S., and Lieberman, H.B.  
952 (2013b). Clamping down on mammalian meiosis. *Cell Cycle* 12, 3135-3145.

953 Mahadevaiah, S.K., Bourc'his, D., de Rooij, D.G., Bestor, T.H., Turner, J.M., and  
954 Burgoine, P.S. (2008). Extensive meiotic asynapsis in mice antagonises meiotic silencing  
955 of unsynapsed chromatin and consequently disrupts meiotic sex chromosome  
956 inactivation. *J Cell Biol* 182, 263-276.

957 Mahadevaiah, S.K., Costa, Y., and Turner, J.M. (2009). Using RNA FISH to study gene  
958 expression during mammalian meiosis. *Methods Mol Biol* 558, 433-444.

959 Miosge, L.A., Sontani, Y., Chuah, A., Horikawa, K., Russell, T.A., Mei, Y., Wagle, M.V.,  
960 Howard, D.R., Enders, A., Tscharke, D.C., *et al.* (2017). Systems-guided forward genetic  
961 screen reveals a critical role of the replication stress response protein ETAA1 in T cell  
962 clonal expansion. *Proc Natl Acad Sci U S A* 114, E5216-E5225.

963 Mordes, D.A., Glick, G.G., Zhao, R., and Cortez, D. (2008). TopBP1 activates ATR  
964 through ATRIP and a PIKK regulatory domain. *Genes Dev* 22, 1478-1489.

965 Ngo, G.H., Balakrishnan, L., Dubarry, M., Campbell, J.L., and Lydall, D. (2014). The 9-1-  
966 1 checkpoint clamp stimulates DNA resection by Dna2-Sgs1 and Exo1. *Nucleic Acids*  
967 *Res* 42, 10516-10528.

968 Ngo, G.H., and Lydall, D. (2015). The 9-1-1 checkpoint clamp coordinates resection at  
969 DNA double strand breaks. *Nucleic Acids Res* 43, 5017-5032.

970 Nguyen, L.T., Schmidt, H.A., von Haeseler, A., and Minh, B.Q. (2015). IQ-TREE: a fast  
971 and effective stochastic algorithm for estimating maximum-likelihood phylogenies. *Mol*  
972 *Biol Evol* 32, 268-274.

973 Pacheco, S., Maldonado-Linares, A., Marcet-Ortega, M., Rojas, C., Martinez-Marchal, A.,  
974 Fuentes-Lazaro, J., Lange, J., Jasin, M., Keeney, S., Fernandez-Capetillo, O., *et al.*  
975 (2018). ATR is required to complete meiotic recombination in mice. *Nat Commun* 9, 2622.

976 Page, S.L., and Hawley, R.S. (2004). The genetics and molecular biology of the  
977 synaptonemal complex. *Annu Rev Cell Dev Biol* 20, 525-558.

978 Pandita, R.K., Sharma, G.G., Laszlo, A., Hopkins, K.M., Davey, S., Chakhronian, M.,  
979 Gupta, A., Wellinger, R.J., Zhang, J., Powell, S.N., *et al.* (2006). Mammalian Rad9 plays  
980 a role in telomere stability, S- and G2-phase-specific cell survival, and homologous  
981 recombinational repair. *Mol Cell Biol* 26, 1850-1864.

982 Pereira, C., Smolka, M.B., Weiss, R.S., and Brieno-Enriquez, M.A. (2020). ATR signaling  
983 in mammalian meiosis: From upstream scaffolds to downstream signaling. *Environ Mol*  
984 *Mutagen* 61, 752-766.

985 Perez-Castro, A.J., and Freire, R. (2012). Rad9B responds to nucleolar stress through  
986 ATR and JNK signalling, and delays the G1-S transition. *J Cell Sci* 125, 1152-1164.

987 Priedigkeit, N., Wolfe, N., and Clark, N.L. (2015). Evolutionary signatures amongst  
988 disease genes permit novel methods for gene prioritization and construction of  
989 informative gene-based networks. *PLoS Genet* 11, e1004967.

990 Rendtlew Danielsen, J.M., Larsen, D.H., Schou, K.B., Freire, R., Falck, J., Bartek, J., and  
991 Lukas, J. (2009). HCLK2 is required for activity of the DNA damage response kinase ATR.  
992 *J Biol Chem* 284, 4140-4147.

993 Romanienko, P.J., and Camerini-Otero, R.D. (2000). The mouse Spo11 gene is required  
994 for meiotic chromosome synapsis. *Mol Cell* 6, 975-987.

995 Royo, H., Polikiewicz, G., Mahadevaiah, S.K., Prosser, H., Mitchell, M., Bradley, A., de  
996 Rooij, D.G., Burgoyne, P.S., and Turner, J.M. (2010). Evidence that meiotic sex  
997 chromosome inactivation is essential for male fertility. *Curr Biol* 20, 2117-2123.

998 Royo, H., Prosser, H., Ruzankina, Y., Mahadevaiah, S.K., Cloutier, J.M., Baumann, M.,  
999 Fukuda, T., Hoog, C., Toth, A., de Rooij, D.G., *et al.* (2013). ATR acts stage specifically  
1000 to regulate multiple aspects of mammalian meiotic silencing. *Genes Dev* 27, 1484-1494.

1001 Sadate-Ngatchou, P.I., Payne, C.J., Dearth, A.T., and Braun, R.E. (2008). Cre  
1002 recombinase activity specific to postnatal, premeiotic male germ cells in transgenic mice.  
1003 *Genesis* 46, 738-742.

1004 Saldivar, J.C., Cortez, D., and Cimprich, K.A. (2017). The essential kinase ATR: ensuring  
1005 faithful duplication of a challenging genome. *Nat Rev Mol Cell Biol* 18, 622-636.

1006 Sanchez, Y., Wong, C., Thoma, R.S., Richman, R., Wu, Z., Piwnica-Worms, H., and  
1007 Elledge, S.J. (1997). Conservation of the Chk1 checkpoint pathway in mammals: linkage  
1008 of DNA damage to Cdk regulation through Cdc25. *Science* 277, 1497-1501.

1009 Shi, B., Xue, J., Yin, H., Guo, R., Luo, M., Ye, L., Shi, Q., Huang, X., Liu, M., Sha, J., et  
1010 *al.* (2019). Dual functions for the ssDNA-binding protein RPA in meiotic recombination.  
1011 *PLoS Genet* 15, e1007952.

1012 Shin, Y.H., Choi, Y., Erdin, S.U., Yatsenko, S.A., Kloc, M., Yang, F., Wang, P.J., Meistrich,  
1013 M.L., and Rajkovic, A. (2010). Hormad1 mutation disrupts synaptonemal complex  
1014 formation, recombination, and chromosome segregation in mammalian meiosis. *PLoS*  
1015 *Genet* 6, e1001190.

1016 Shinohara, M., Bishop, D.K., and Shinohara, A. (2019). Distinct Functions in Regulation  
1017 of Meiotic Crossovers for DNA Damage Response Clamp Loader Rad24(Rad17) and  
1018 Mec1(ATR) Kinase. *Genetics* 213, 1255-1269.

1019 Shinohara, M., Hayashihara, K., Grubb, J.T., Bishop, D.K., and Shinohara, A. (2015).  
1020 DNA damage response clamp 9-1-1 promotes assembly of ZMM proteins for formation  
1021 of crossovers and synaptonemal complex. *J Cell Sci* 128, 1494-1506.

1022 Sims, J.R., Faça, V.M., Pereira, C., Arroyo-Martinez, G.A., Cohen, P.E., Weiss, R.S., and  
1023 Smolka1, M.B. (2021). Phosphoproteomics of ATR Signaling in Prophase I of Mouse  
1024 Meiosis

1025 Turner, J.M. (2007). Meiotic sex chromosome inactivation. *Development* 134, 1823-1831.

1026 Turner, J.M. (2015). Meiotic Silencing in Mammals. *Annu Rev Genet* 49, 395-412.

1027 Turner, J.M., Aprelikova, O., Xu, X., Wang, R., Kim, S., Chandramouli, G.V., Barrett, J.C.,  
1028 Burgoyne, P.S., and Deng, C.X. (2004). BRCA1, histone H2AX phosphorylation, and  
1029 male meiotic sex chromosome inactivation. *Curr Biol* 14, 2135-2142.

1030 Vasileva, A., Hopkins, K.M., Wang, X., Weisbach, M.M., Friedman, R.A., Wolgemuth,  
1031 D.J., and Lieberman, H.B. (2013). The DNA damage checkpoint protein RAD9A is  
1032 essential for male meiosis in the mouse. *J Cell Sci* 126, 3927-3938.

1033 Visnes, T., Giordano, F., Kuznetsova, A., Suja, J.A., Lander, A.D., Calof, A.L., and Strom,  
1034 L. (2014). Localisation of the SMC loading complex Nipbl/Mau2 during mammalian  
1035 meiotic prophase I. *Chromosoma* 123, 239-252.

1036 Ward, A., Hopkins, J., McKay, M., Murray, S., and Jordan, P.W. (2016). Genetic  
1037 Interactions Between the Meiosis-Specific Cohesin Components, STAG3, REC8, and  
1038 RAD21L. *G3 (Bethesda)* 6, 1713-1724.

1039 Weiss, R.S., Enoch, T., and Leder, P. (2000). Inactivation of mouse Hus1 results in  
1040 genomic instability and impaired responses to genotoxic stress. *Genes Dev* 14, 1886-  
1041 1898.

1042 Widger, A., Mahadevaiah, S.K., Lange, J., Ellnati, E., Zohren, J., Hirota, T., Pacheco, S.,  
1043 Maldonado-Linares, A., Stanzione, M., Ojarikre, O., *et al.* (2018). ATR is a multifunctional  
1044 regulator of male mouse meiosis. *Nat Commun* 9, 2621.

1045 Wit, N., Krijger, P.H., van den Berk, P.C., and Jacobs, H. (2011). Lysine residue 185 of  
1046 Rad1 is a topological but not a functional counterpart of lysine residue 164 of PCNA.  
1047 *PLoS One* 6, e16669.

1048 Wojtasz, L., Daniel, K., Roig, I., Bolcun-Filas, E., Xu, H., Boonsanay, V., Eckmann, C.R.,  
1049 Cooke, H.J., Jasin, M., Keeney, S., *et al.* (2009). Mouse HORMAD1 and HORMAD2, two  
1050 conserved meiotic chromosomal proteins, are depleted from synapsed chromosome axes  
1051 with the help of TRIP13 AAA-ATPase. *PLoS Genet* 5, e1000702.

1052 Wolfe, N.W., and Clark, N.L. (2015). ERC analysis: web-based inference of gene function  
1053 via evolutionary rate covariation. *Bioinformatics* 31, 3835-3837.

1054 Zhang, B., Tang, Z., Li, L., and Lu, L.Y. (2020). NBS1 is required for SPO11-linked DNA  
1055 double-strand break repair in male meiosis. *Cell Death Differ.*

1056 Zickler, D., and Kleckner, N. (2015). Recombination, Pairing, and Synapsis of Homologs  
1057 during Meiosis. *Cold Spring Harb Perspect Biol* 7.

1058 Zou, L. (2003). Sensing DNA Damage Through ATRIP Recognition of RPA-ssDNA  
1059 Complexes. *Science* 300, 1542-1548.

1060

1061 **Table 1: Analysis of epididymal sperm counts and fertility in *Rad1* CKO and control**  
1062 **mice<sup>1</sup>.**

Genotype	# males	Epididymal Sperm Count (x10 <sup>6</sup> )	# matings	# copulatory plugs	# pregnancies	Total viable pups
Control	3	16.6 ± 4.5	12	12	10	66
<i>Rad1</i> CKO	3	0.0 ± 0	15	15	0	0

1063  
1064 <sup>1</sup> Male *Rad1* CKO mice at 8 to 12 weeks of age were bred to 6-week-old wild-type FVB  
1065 female mice.

1066

1067 **KEY RESOURCES TABLE**

Antibody	Source	Concentration
<b>Rabbit anti-RAD1</b>	R. S. Weiss (HM454) (Lyndaker et al., 2013a)	1:100
<b>Rabbit anti-RAD9B</b>	R. Freire (Perez-Castro and Freire, 2012)	1:100
<b>Rabbit anti-RAD9A</b>	R. S. Weiss (HM456) (Lyndaker et al., 2013a)	1:100
<b>Mouse anti-<math>\gamma</math>H2AX</b>	Millipore (05-363)	1:1000
<b>Mouse anti-SYCP3</b>	Abcam (ab97672)	1:1000
<b>Rabbit anti-SYCP3</b>	P. Cohen	1:1000
<b>Rabbit anti-SYCP1</b>	Abcam (ab15090)	1:1000
<b>Rabbit anti-RAD51</b>	Millipore (PC130)	1:1000
<b>Rabbit anti-RPA2</b>	J. Wang (UP2436) (Shi et al., 2019)	1:500
<b>Rabbit anti-MEIOB</b>	J. Wang (UP2327) (Luo et al., 2013)	1:500
<b>Rabbit anti-ATR</b>	Cell Signaling (2790)	1:100
<b>Rabbit anti-TOPBP1</b>	R. Freire (Rendtlew Danielsen et al., 2009)	1:500
<b>Rabbit anti-pCHK1 (S317)</b>	Cell Signaling (12302S)	1:100
<b>Mouse anti-MLH1</b>	BD Sciences (550838)	1:1000
<b>Guinea pig anti-H1T</b>	M. A. Handel (Inselman et al., 2003)	1:500

<b>Rabbit anti-pHORMAD2 (S271)</b>	A. Toth (AB324) (Wojtasz et al., 2009)	1:500
<b>Rabbit anti-HORMAD2</b>	A. Toth (AB211) (Wojtasz et al., 2009)	1:500
<b>Rabbit anti-HORMAD1</b>	A. Toth (AB334) (Wojtasz et al., 2009)	1:500
<b>Rabbit anti-SMC3</b>	Bethyl (A300-060A)	Spreads- 1:100 WB- 1:1000
<b>Rabbit anti-pSMC3 (S1038)</b>	Bethyl (IHC-0070)	Spreads- 1:100 WB- 1:1000
<b>Mouse anti-GAPDH</b>	Invitrogen (AM4300)	1:5000
<b>Mouse anti-ACTIN</b>	Cell Signaling (4967S)	1:5000
<b>Mouse anti-FLAG</b>	Sigma (F1804)	1:5000
<b>Mouse anti-MYC</b>	Cell Signaling (2276S)	1:5000
<b>Mouse anti- HA</b>	BioLegend (901501)	1:5000
<b>Goat anti-rabbit Alexafluor 488</b>	Invitrogen (A11034)	1:1000
<b>Goat anti-mouse Alexafluor 488</b>	Invitrogen (A-11017)	1:1000
<b>Goat anti-rabbit Alexafluor 594</b>	Invitrogen (A11012)	1:1000
<b>Goat anti-mouse Alexafluor 594</b>	Invitrogen (PIA32742)	1:1000
<b>Goat anti-guinea pig Alexafluor 555</b>	Invitrogen (A21450)	1:1000

1069

Primers	Sequence	Source
<b>Cre ic318R</b>	AGGGACACAGCATTGGAGTC	IDT
<b>Cre ic202F</b>	GTGCAAGCTGAACAACAGGA	IDT
<b>Rad1 G1 F</b>	AGGTACGTCAGTGCGATTACCCT	IDT
<b>Rad1 G3 R</b>	CCCTCAAGATGTAACCTCATCTAC	IDT
<b>Hus1 3.107</b>	GGGCTGATGCGGAGGGTGCAGGTT	IDT
<b>Hus1 Neo1</b>	GCTCTTACTGAAGGCTCTTAC	IDT
<b>Hus1 5-OSMCS2</b>	GCGAAGACGGAATTGATCAGGCCACG	IDT
<b>Hus1 5.-20</b>	CCGTCGGCCTGGTATCCGCCATGA	IDT
<b>Hus1 3.159</b>	CTCACAACTGCTACAAGGTTAGGC	IDT

1070

## 1071 KEY RESOURCES TABLE REFERENCES

1072 Inselman, A., Eaker, S., and Handel, M.A. (2003). Temporal expression of cell cycle-  
1073 related proteins during spermatogenesis: establishing a timeline for onset of the meiotic  
1074 divisions. *Cytogenet Genome Res* 103, 277-284.

1075 Luo, M., Yang, F., Leu, N.A., Landaiche, J., Handel, M.A., Benavente, R., La Salle, S.,  
1076 and Wang, P.J. (2013). MEIOB exhibits single-stranded DNA-binding and exonuclease  
1077 activities and is essential for meiotic recombination. *Nat Commun* 4, 2788.

1078 Lyndaker, A.M., Lim, P.X., Mleczko, J.M., Diggins, C.E., Holloway, J.K., Holmes, R.J.,  
1079 Kan, R., Schlafer, D.H., Freire, R., Cohen, P.E., *et al.* (2013). Conditional inactivation of  
1080 the DNA damage response gene Hus1 in mouse testis reveals separable roles for  
1081 components of the RAD9-RAD1-HUS1 complex in meiotic chromosome maintenance.  
1082 *PLoS Genet* 9, e1003320.

1083 Perez-Castro, A.J., and Freire, R. (2012). Rad9B responds to nucleolar stress through  
1084 ATR and JNK signalling, and delays the G1-S transition. *J Cell Sci* 125, 1152-1164.

1085 Rendtlew Danielsen, J.M., Larsen, D.H., Schou, K.B., Freire, R., Falck, J., Bartek, J., and  
1086 Lukas, J. (2009). HCLK2 is required for activity of the DNA damage response kinase ATR.  
1087 *J Biol Chem* 284, 4140-4147.

1088 Shi, B., Xue, J., Yin, H., Guo, R., Luo, M., Ye, L., Shi, Q., Huang, X., Liu, M., Sha, J., et  
1089 *al.* (2019). Dual functions for the ssDNA-binding protein RPA in meiotic recombination.  
1090 *PLoS Genet* 15, e1007952.

1091 Wojtasz, L., Daniel, K., Roig, I., Bolcun-Filas, E., Xu, H., Boonsanay, V., Eckmann, C.R.,  
1092 Cooke, H.J., Jasin, M., Keeney, S., *et al.* (2009). Mouse HORMAD1 and HORMAD2, two  
1093 conserved meiotic chromosomal proteins, are depleted from synapsed chromosome axes  
1094 with the help of TRIP13 AAA-ATPase. *PLoS Genet* 5, e1000702.

1095

Pereira\_Fig1

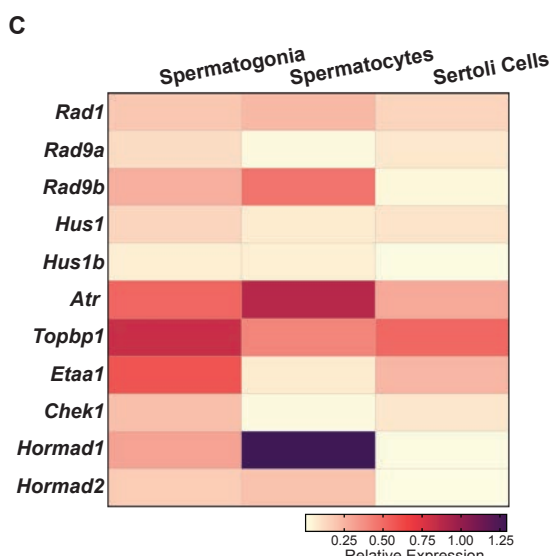
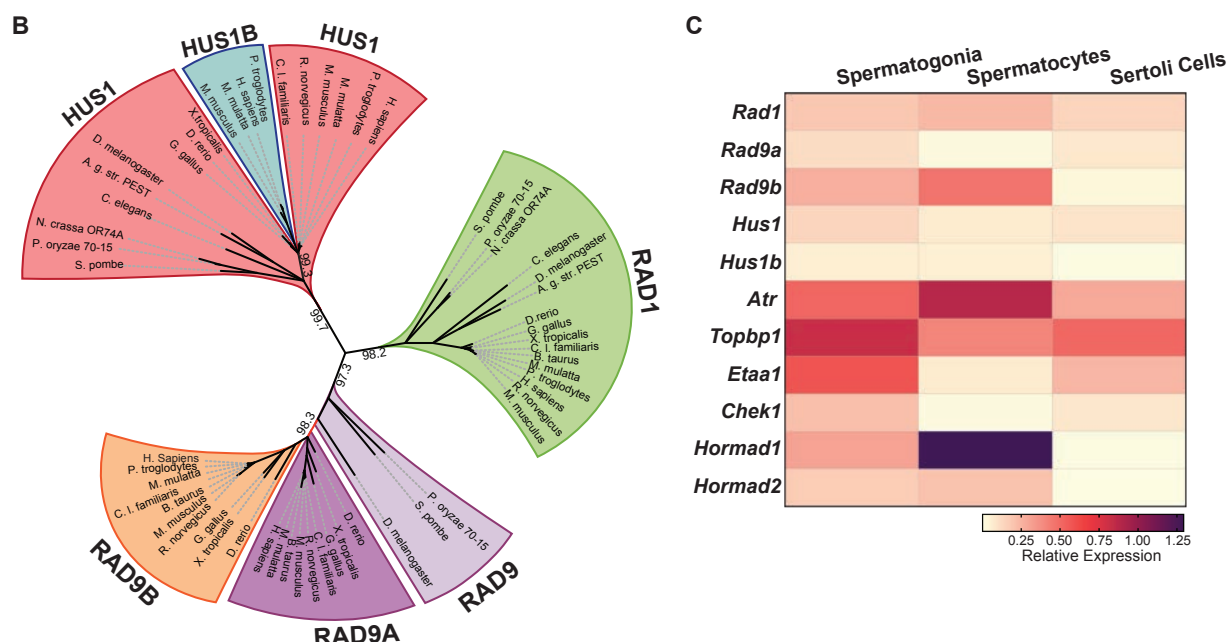
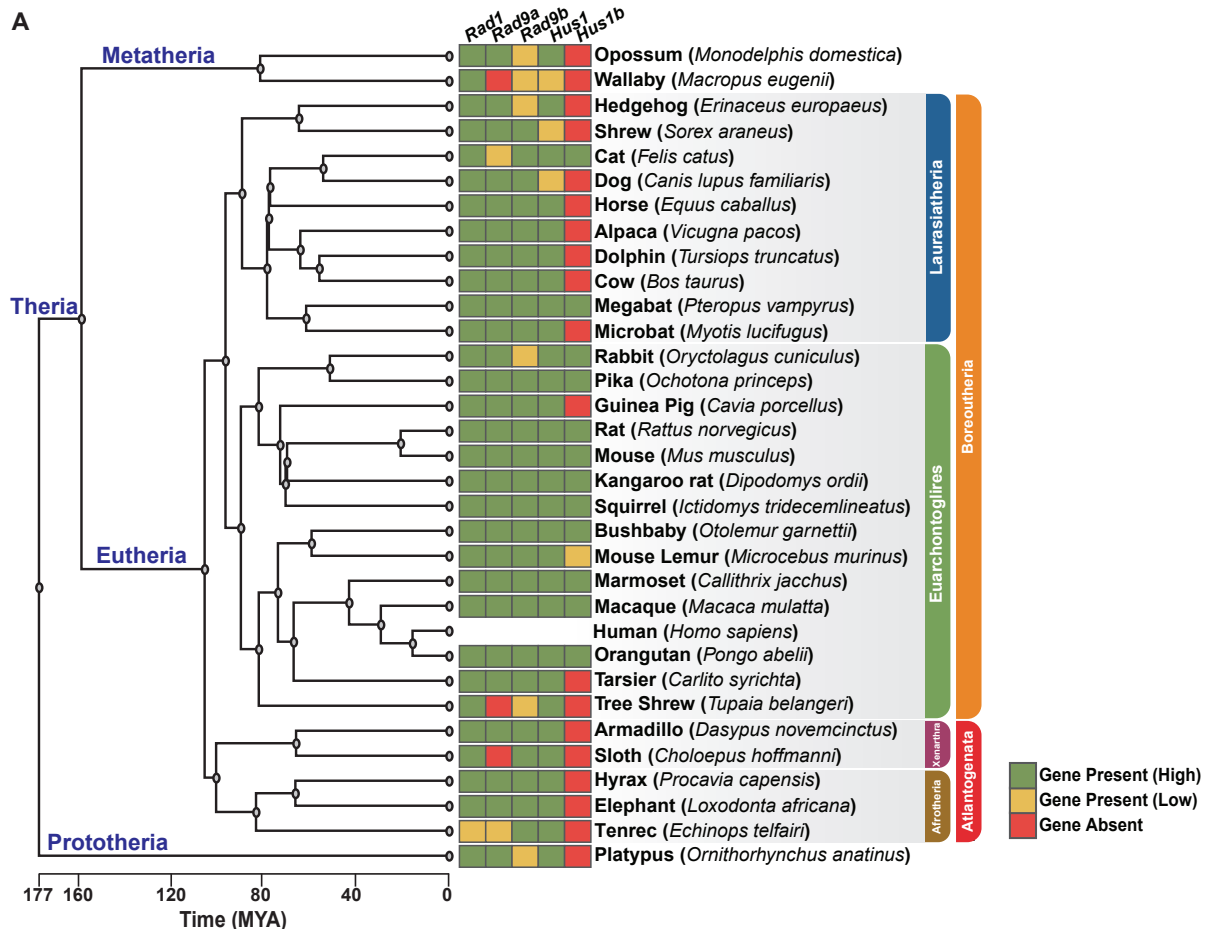


**Figure 1: Phylogenetic analysis of 9-1-1 complex subunits.** (A) Gene presence and absence matrix of human 9-1-1 subunit orthologue genes in 33 representative mammals. High confidence was determined if the genomic sequence had  $\geq 50\%$  of both target and query sequence identity, and a pairwise whole genomic alignment score of  $\geq 50$  when compared to human or if the genomic region containing the gene was syntenic with human. If an ortholog did not reach the threshold then it was annotated as low confidence (yellow). If no ortholog was found, then it was considered absent (red). A Cladogram was obtained from timetree.org. (B) Maximum likelihood unrooted phylogenetic tree of 9-1-1 subunit genes based on JTT+I+G+F. Protein sequences were obtained from NCBI HomoloGene and include: bacteria (*Pleomorphomonas oryzae*), fungi (*Schizosaccharomyces pombe*, *Neurospora crassa*), nematode (*Caenorhabditis elegans*), true flies (*Drosophila melanogaster*, *Anopheles gambiae str. Pest*), fish (*Danio rerio*), frog (*Xenopus tropicalis*), bird (*Gallus gallus*), carnivora (*Canis lupus*), rodents (*Rattus norvegicus*, *Mus musculus*) and primates (*Homo sapiens*, *Mus musculus*, *Macaca mulatta*, *Pan troglodytes*). Sequences were aligned by Clustal Omega and substitution model was tested on ProtTest. Ultrafast bootstrap (x1000 replicates) was performed in IQ-TREE web server and nodes below 70% branch support were collapsed. Branch distance represents substitution rate. (C) Heatmap of single cell RNA sequencing data from mouse testes was queried to assess the expression of 9-1-1 subunits, *Atr*, *Topbp1*, *Etaa1*, *Chk1*, *Hormad1* and *Hormad2* in spermatogonia, spermatocytes and Sertoli cells. Expression of *Rad9b* in spermatocytes p value  $\leq 5.47e^{-10}$ , *Hus1b* p value  $\leq 1.20e^{-09}$ , *Rad1* p value  $\leq 1.08e^{-08}$ . Expression of *Rad9a* and *Hus1* in spermatogonia p value  $\leq 5.61e^{-19}$ ; p

value  $\leq 3.78e^{-09}$ . Relative expression is shown of each gene, highest expression observed in purple and lowest expression observed in yellow.

## Pereira\_Fig1\_supplement1

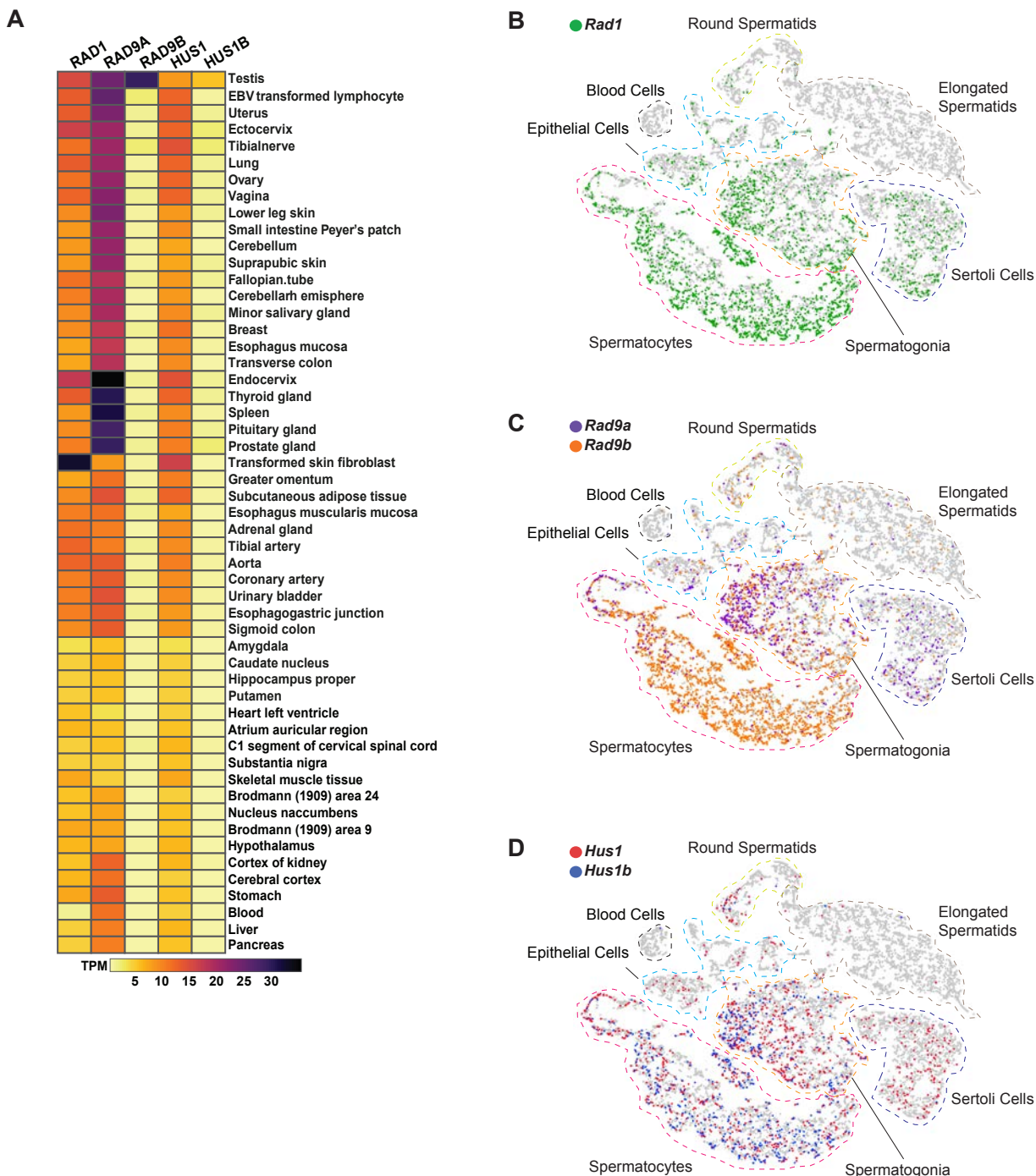


**Figure 1 Supplement 1: Expression of 9-1-1 complex subunits.** (A) Expression of 9-1-1 subunits in various human tissues. Data from the Genotype-Tissue Expression (GTEx) project was obtained in Expression Atlas – EMBL-EBI. Gene expression values are shown as transcript per million (TPM). (B-D) tSNE plots of single-cell RNA seq analysis of mouse testes demonstrating the expression of 9-1-1 subunits in single cells from round spermatids, elongated spermatids, blood cells, epithelial, spermatocytes, spermatogonia, and Sertoli cells population within testes. Gray circles are individual cells. *Rad1*-expressing cells are shown in green (B). *Rad9a*-expressing cells are shown in purple, and *Rad9b*-expressing cells are in orange (C). *Hus1*-expressing cells are in red, and *Hus1b*-expressing cells are in blue (D).

Pereira\_Fig2

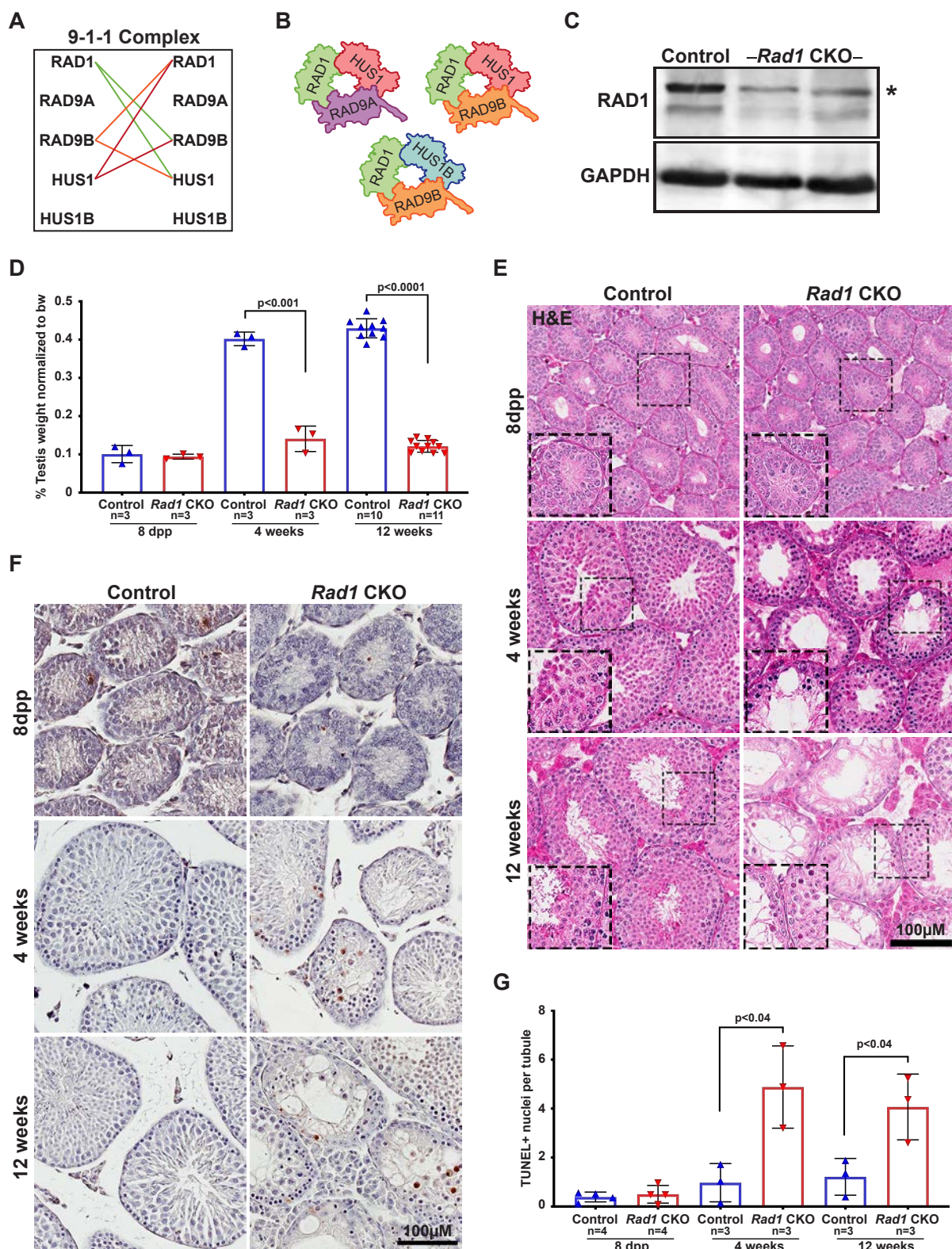


**Figure 2: Conditional knockout targeting multiple 9-1-1 complexes causes severe germ cell loss in testes.** (A) Evolutionary rate covariation analysis between 9-1-1 subunits. Lines depict significant covariance between 9-1-1 subunits. (B) Schematic showing putative meiotic 9-1-1 complexes: 9A-1-1, 9B-1-1 and 9B-1-1B. (C) Immunoblotting for RAD1 in control and *Rad1* CKO whole testes lysates from 12-week-old mice. (D) Testis weight normalized to body weight from 8-dpp, 4-week-old, and 12-week-old control and *Rad1* CKO mice. (E) Seminiferous tubule cross sections from 8 day postpartum (dpp), 4-week-old and 12-week-old mice were stained with H&E (representative images from 3 mice analyzed per age group per genotype). (F-G) Representative images (F) and quantification (G) of TUNEL positive cells per tubule in control and *Rad1* CKO mice (50 tubules per mouse quantified; n= number of mice analyzed). p-value calculated using Welch's unpaired t-test using Graphpad.

Pereira\_Fig2\_supplement1

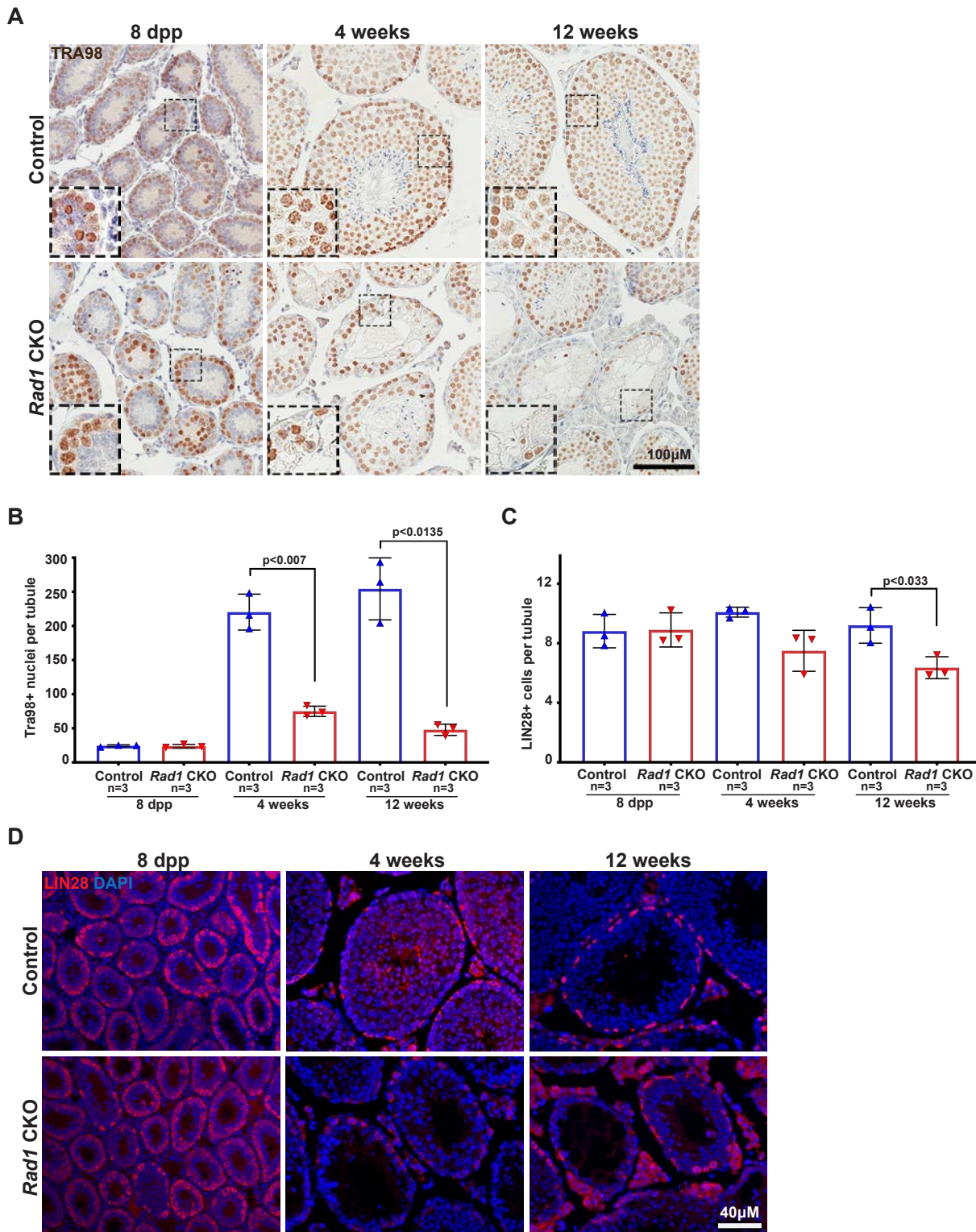


**Figure 2 Supplement 1: *Rad1* inactivation in testis causes germ cell loss. (A-B)**

Representative images (A) and quantification (B) of TRA98-positive cells per tubule in control and *Rad1* CKO mice (n= number of mice; 50 tubules per mouse quantified). (C-D) Representative images (C) and quantification (D) of LIN28-positive spermatogonial stem cells (n= number of mice; 50 tubules per mouse quantified). p-value calculated using Welch's unpaired t-test in Graphpad Prism8.

Pereira\_Fig3

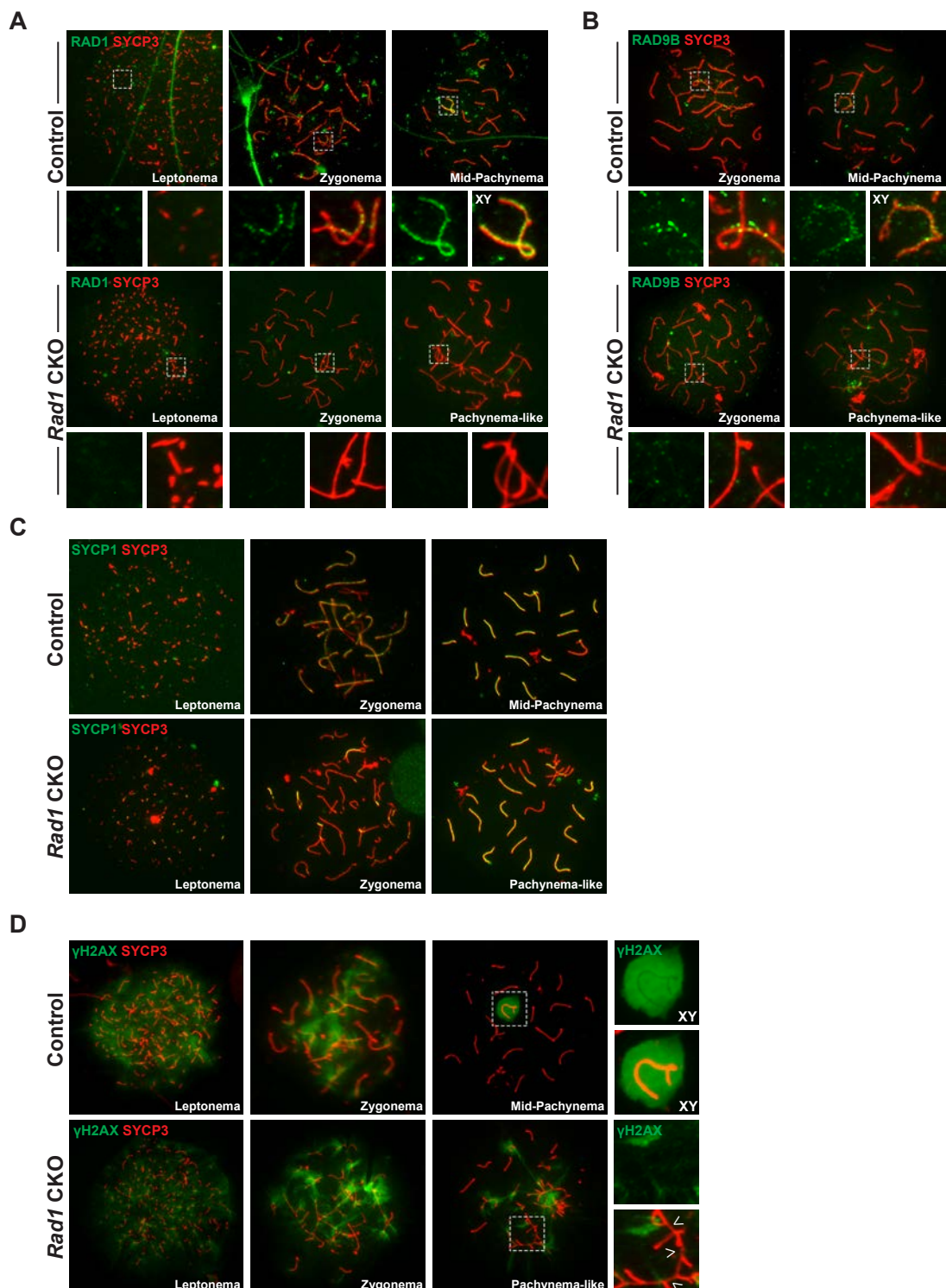


**Figure 3: Increased asynapsis and DNA damage is observed upon testis-specific RAD1 loss.** (A-B) Meiotic spreads from 12-week-old control and *Rad1* CKO mice stained for RAD1 (A) or RAD9B (B). (C) Co-staining of SYCP1 and SYCP3 from 12-week-old control and *Rad1* CKO mice (3 control mice, n= 156 cells; 3 CKO mice, n= 131 cells). *Rad1* CKO meiocytes with 4 or more synapsed chromosomes were categorized as pachytene-like. (D)  $\gamma$ H2AX staining of meiotic spreads from control and *Rad1* CKO mice. Arrowheads in *Rad1* CKO spreads highlight regions of asynapsis lacking  $\gamma$ H2AX staining (3 control mice, n= 127 cells; 5 CKO mice, n= 205 cells). P-values were calculated using Welch's unpaired t-test using Graphpad.

Pereira\_Fig3\_supplement1

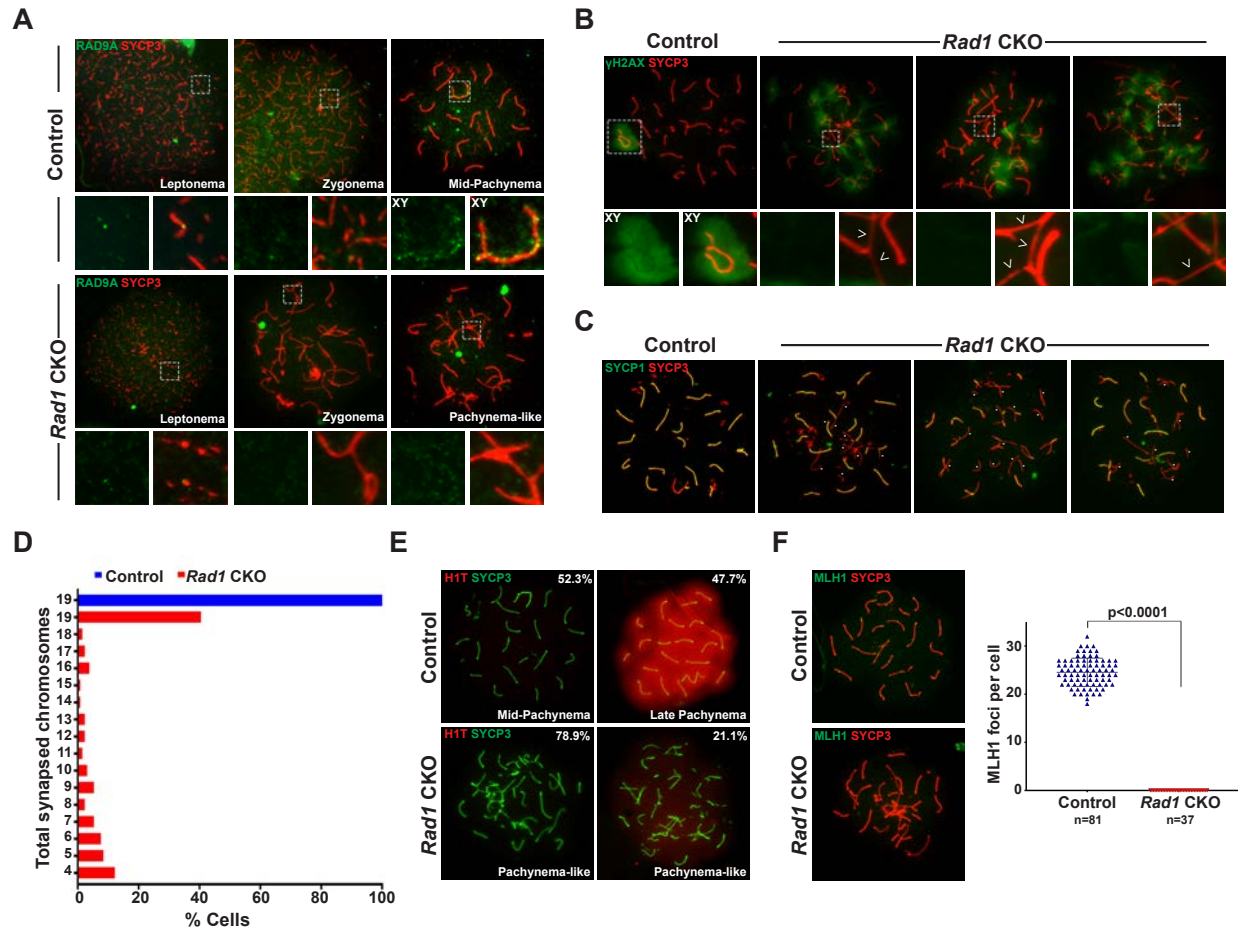


**Figure 3 Supplement 1: *Rad1 CKO* spermatocytes show RAD9A loss and do not progress to mid-pachynema.** (A) Representative meiotic spread images stained for RAD9A from control and *Rad1 CKO* 12-week-old mice (3 control mice; n= 178 cells; 3 CKO mice; n=81 cells). (B) Additional examples of yH2AX meiotic spread staining in control and *Rad1 CKO* mice (3 control mice; n= 127 cells; 5 CKO mice; n=205 cells). (C) Examples of SYCP1/3 co-staining in control and *Rad1 CKO* meiotic spreads, asterisks indicate properly synapsed chromosomes (3 control mice; n= 156 cells; 3 CKO mice; n=131 cells). (D) Total synapsed chromosomes per cell in control (blue) and *Rad1 CKO*

(red) per cell (3 control mice; n= 156 cells; 3 CKO mice; n=131 cells). (E) H1T meiotic spread staining from control and *Rad1* CKO mice. Of 174 pachynema staged cells analyzed from control mice 52.3% cells showed no H1T staining (2 control mice). 104 pachynema-like staged cells from *Rad1* CKO mice were analyzed with 78.9% of cells displaying no H1T and 21.1% showed low levels of H1T staining (2 CKO mice). (F) Representative images of MLH1 staining in control and *Rad1* CKO spreads, and quantification of MLH1 foci (D) (2 control mice; n= 81 cells; 2 *Rad1* CKO mice; n=37 cells). p-value calculated using Welch's unpaired t-test using Graphpad Prism8.

Pereira\_Fig4

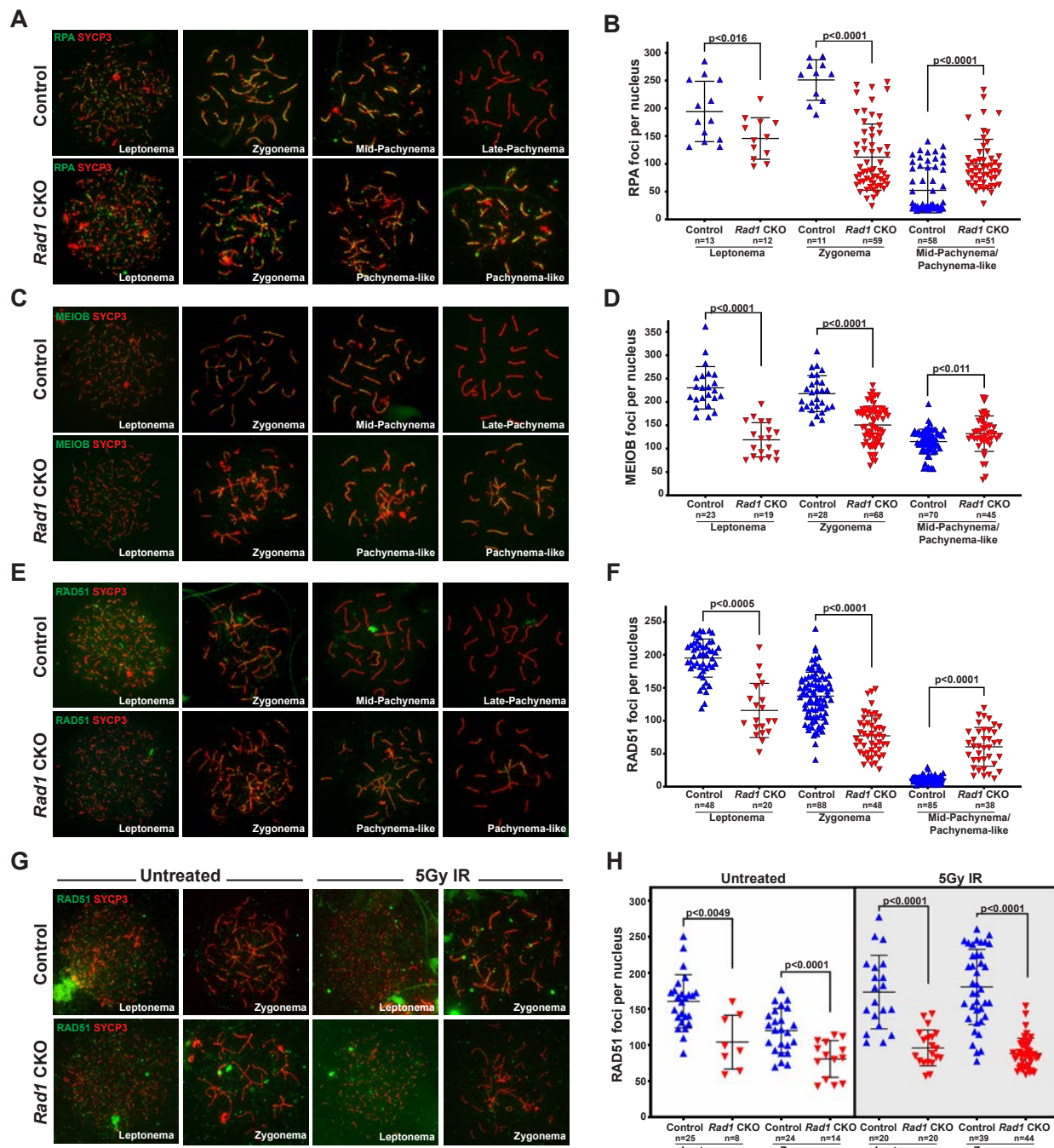


**Figure 4: DSB repair is compromised in the absence of 9-1-1 complexes. (A-B)**

Representative images (A) and quantification (B) of RPA staining of meiotic spreads from 12-week-old control and *Rad1* CKO mice (3 mice per genotype analyzed; n=total cells

analyzed). (C-D) Representative meiotic spread images for ssDNA marker MEIOB (C) and quantifications (D) from 12-week-old control and *Rad1* CKO mice (3 mice per genotype analyzed; n= total cells analyzed). (E-F) Representative meiotic spread images of RAD51 (E) and quantifications (F) from 12-week-old control and *Rad1* CKO mice (5 control mice and 6 CKO analyzed; n=total cells analyzed). (G-H) 8-week-old control and *Rad1* CKO mice were irradiated with 5Gy IR and collected 1-hour post IR. Representative RAD51 meiotic spread images (G) and quantifications (H) (2 control mice and 2 CKO analyzed; n= total cells analyzed). P-values were calculated using Welch's unpaired t-test using Graphpad.

## Pereira\_Fig4\_supplement1

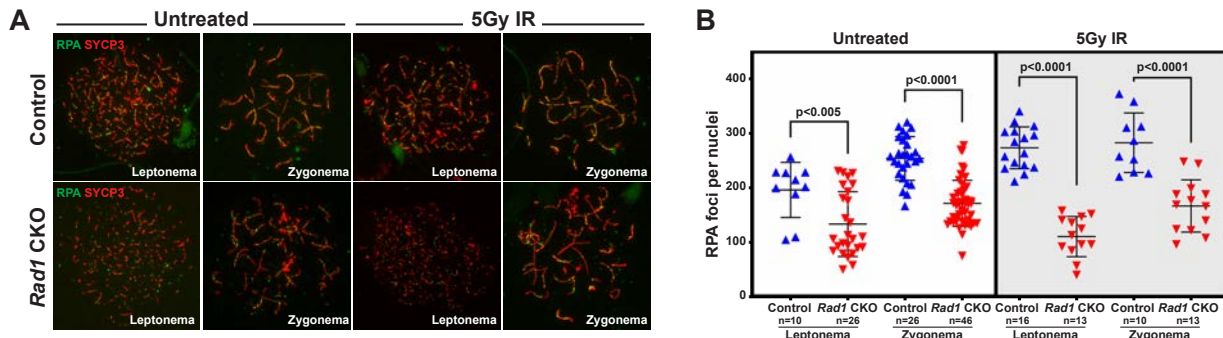


**Figure 4 Supplement 1: Repair of IR-induced DSBs during early prophase I is compromised in the absence of 9-1-1 complexes.** 8-week-old control and *Rad1* CKO mice were irradiated with 5Gy IR and collected 1-hour post IR. (A and B) Representative images (A) and quantification (B) of RPA staining of meiotic spreads prepared from mice of the indicated genotypes (2 control mice and 2 CKO analyzed; n=total cells analyzed). (C and D) MEIOB representative meiotic spreads images (C) and quantifications (D) (2 control mice and 2 CKO analyzed; n=total cells analyzed). p-value calculated using Welch's unpaired t-test using Graphpad Prism8.

Pereira\_Fig5

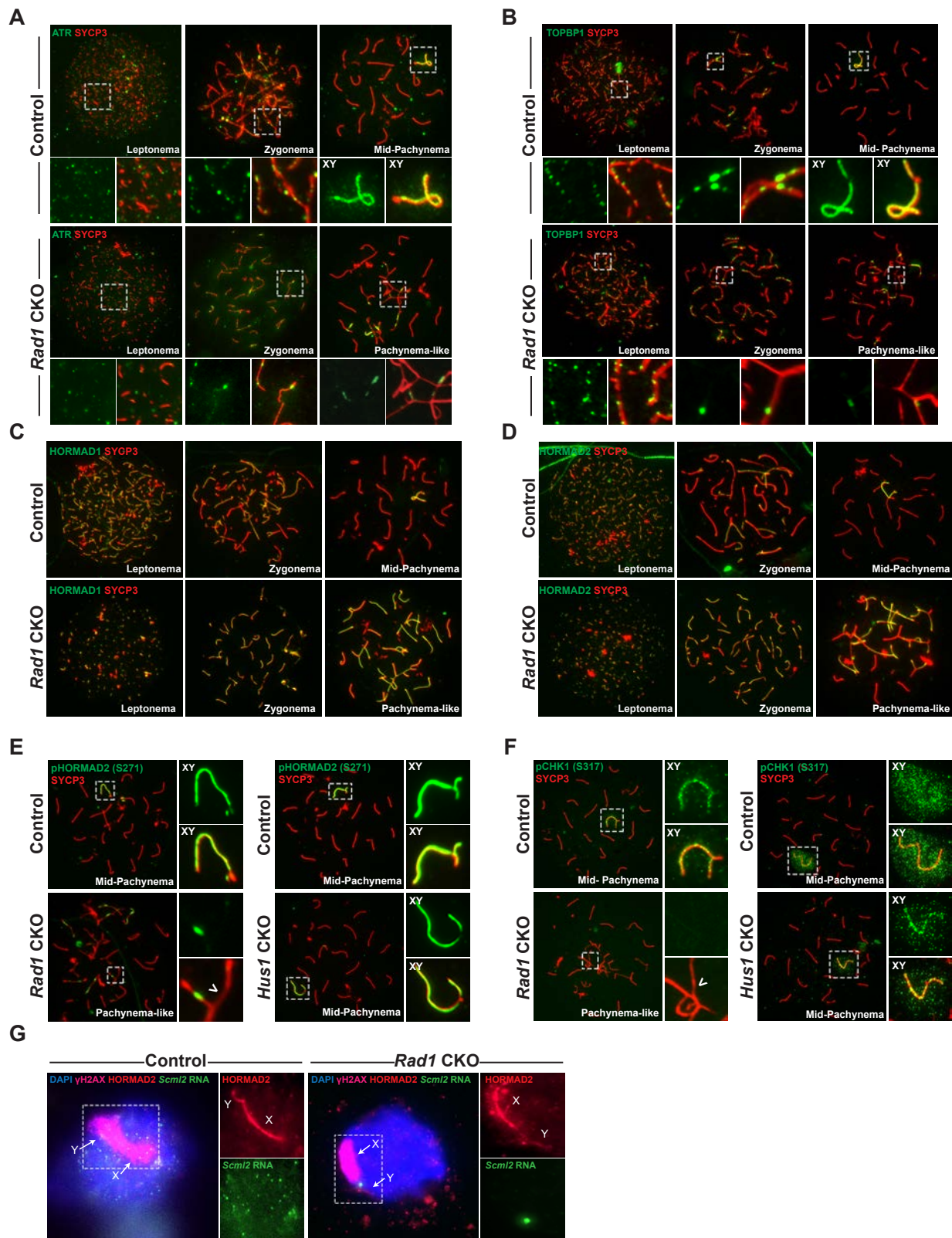


**Figure 5: ATR localization and function is dependent upon 9-1-1 complexes.** (A) ATR localization in control and *Rad1* CKO 12-week-old meiotic spreads (3 control, n= 171 cells; 3 CKO, n= 146). (B) Representative images of TOPBP1 localization in meiotic spreads from 12-week-old control and *Rad1* CKO mice (3 control, n= 130 cells; 3 CKO, n= 129). (C-D) Representative images of HORMAD1 and HORMAD2 localization in 12-week-old control and *Rad1* CKO mice (3 control, n= 146; 3 CKO, n= 119). (E) Representative images of phospho-HORMAD2 (S271) localization in 12-week-old control and *Rad1* CKO mice (*Rad1* CKO: 3 control, n= 178; 3 CKO, n= 146. *Hus1* CKO: 2 control, n= 189; 3 CKO, n= 145). (F) Representative images of phospho-CHK1 (S317) localization in *Rad1* CKO and *Hus1* CKO mice (*Rad1* CKO: 3 control, n= 125; 3 CKO, n= 120. *Hus1* CKO: 2 control, n= 107; 3 CKO, n= 191). (G) RNA FISH for *Scml2* in fully synapsed, pachytene-stage control and *Rad1* CKO cells (3 control, n= 29 cells; 3 CKO, n= 45 cells).

Pereira\_Fig6

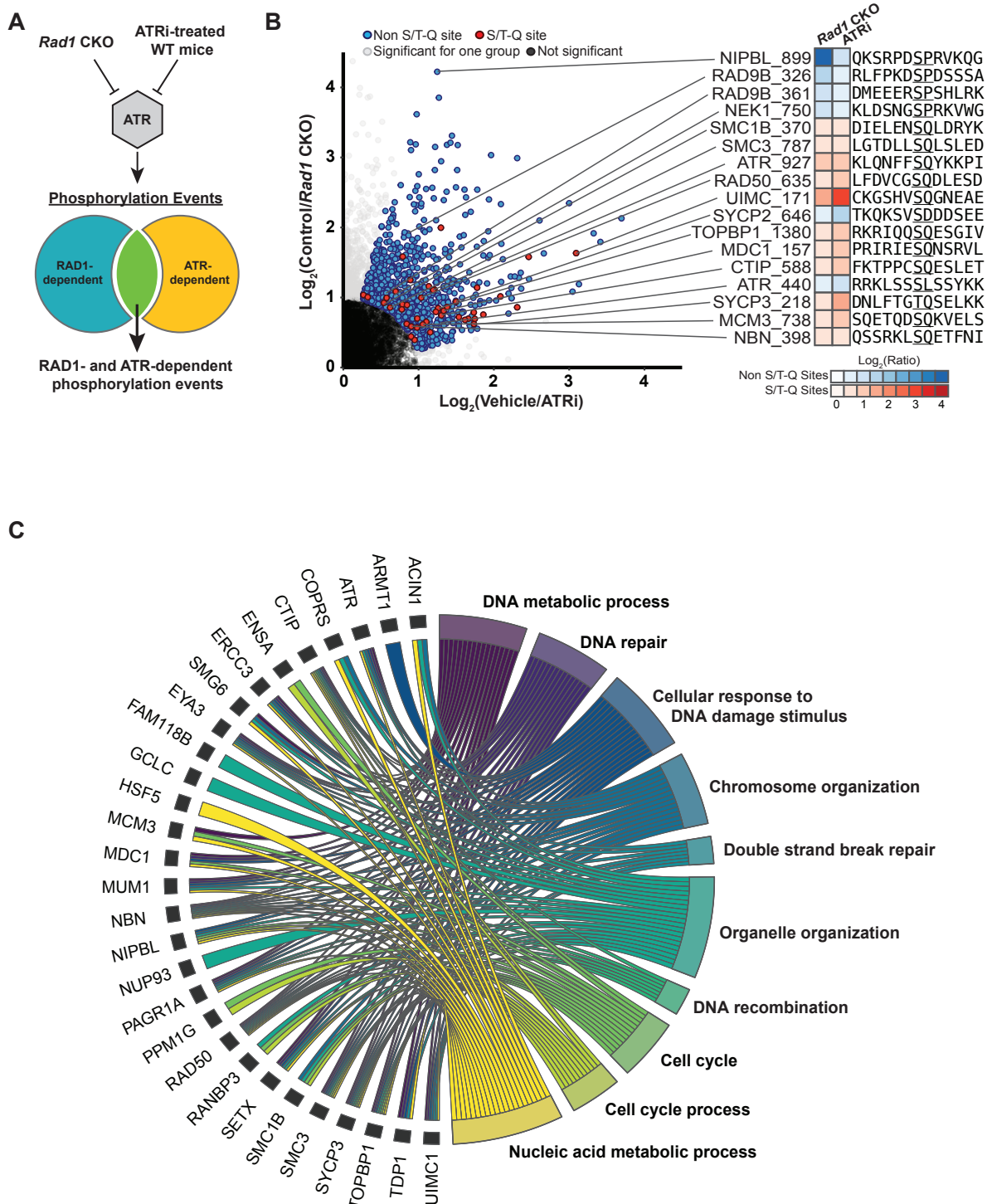


**Figure 6: Coordinated roles for 9-1-1 complexes and ATR in phospho-regulation of DDR and cohesin proteins.** (A) Decapsulated testes from adult *Rad1* CKO mice or WT C57BL/6 mice treated with ATRi were subjected to phosphoproteome analysis. Subsequent analyses focused on proteins phosphorylated in a RAD1- and ATR-dependent manner. (B) Bowtie analysis showed a total of 863 ATR/RAD1-dependent phosphorylation events detected. Red circles indicate S/T-Q sites (42 peptides), blue are non-S/T-Q sites, gray are significant phosphosites in either only the ATRi or the *Rad1* CKO experiment, and black circles were phosphosites in both experiments but were not differentially phosphorylated. For the indicated phosphoproteins, the heatmap shows the average of the log2 fold change across replicates for each experiment (ATRi and *Rad1* CKO), and the amino acid sequence shows 6 residues upstream and 6 residues downstream from the indicated phosphosite. (C) Gene ontology analysis of ATR/RAD1-dependent S/T-Q phosphorylation events was done using STRINGdb. The top ten significantly enriched biological processes GO terms were selected and represented as a chord diagram. GO terms are shown on the right and proteins found for each term on the left.

Pereira\_Fig7

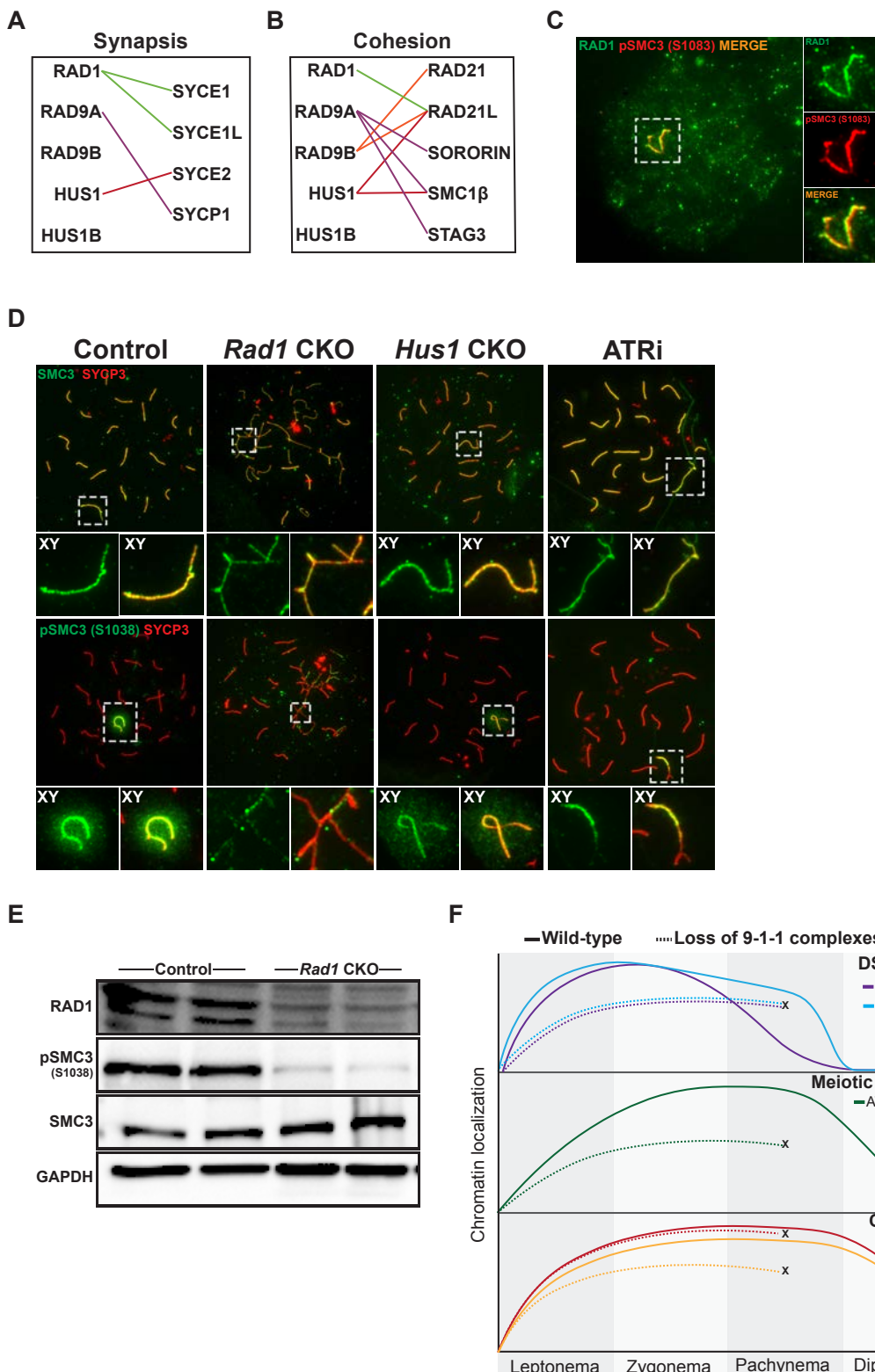


**Figure 7: Cohesin phosphorylation events are dependent upon the 9-1-1/ATR axis.**

(A-B) ERC analysis between 9-1-1 complex subunits and synaptonemal complex (A) and cohesin (B) factors. Lines depict significant correlations observed between 9-1-1 complex subunits and synapsis or cohesin factors. (C) Co-staining of RAD1 and pSMC3 (1083) in wild-type spermatocytes. (D) Representative images of SMC3 and pSMC3 (1038) localization in pachynema and pachytene-like cells from control, *Rad1* CKO, *Hus1* CKO and ATRi-treated mice. (E) Representative immunoblot for phosphorylated SMC3 and total SMC3 in whole testes lysates from 12-week-old control and *Rad1* mice. (F) Summary graphic depicting the localization of key meiotic factors in wild-type versus *Rad1* CKO spermatocytes. Loss of 9-1-1 complexes resulted in early-to-mid pachynema arrest, as depicted by the 'X'. DSB repair markers, such as RAD51, were reduced in the absence of the 9-1-1 complexes. Meiotic silencing factors such as ATR and TOPBP1 also failed to localize properly in the absence of the 9-1-1 complexes. The cohesin subunit SMC3 localized properly in the absence of 9-1-1 subunits but its phosphorylation was impaired in *Rad1* CKO spermatocytes.

Pereira\_Fig7\_supplement1

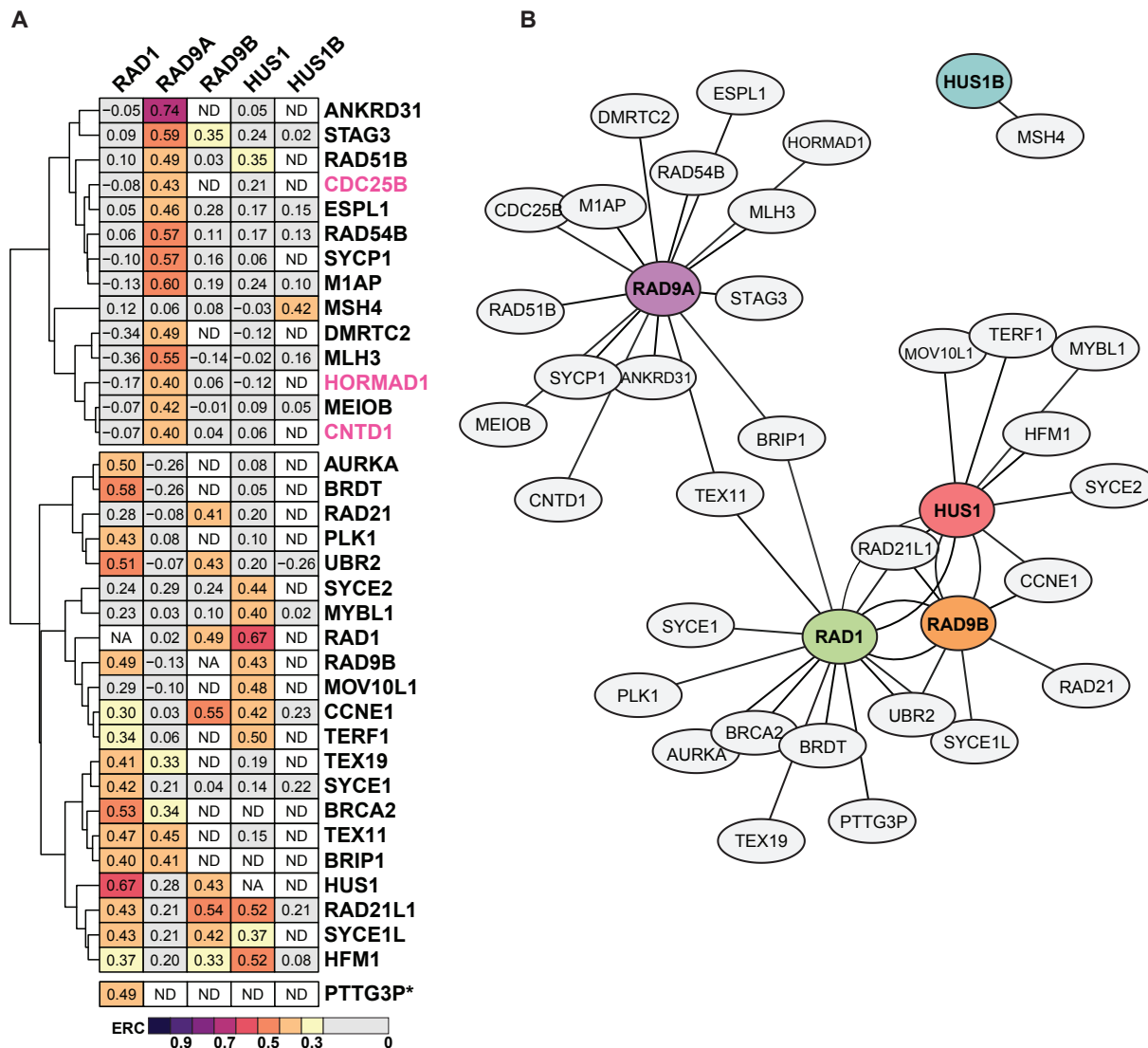


**Figure 7 Supplement 1: Evolutionary rate covariation network of meiosis I proteins.**

(A) Heatmap of proteins found under Gene ontology term meiosis I (GO:0007127) that showed ERC values  $\geq 0.4$  for each subunit. Pink labeling denotes proteins with no significant ERC values ( $p>0.05$ ). ND: no value exists in dataset for paired comparison between the two proteins. NA: not applicable for comparisons between the same protein. PTTG3P\* has a high ERC and significance with RAD1 only. (B) ERC values between subunits and meiosis I proteins were used to plot the network with force-directed layout.

The Fruchterman & Reingold algorithm features attraction between highly connected nodes, identifying protein clusters based on ERC data. The distance between nodes is proportional to absolute edge weight (ERC value of each protein), with shorter distances between nodes reflecting higher ERC values.